Electronic Supplementary Material (ESI) for Journal of Materials Chemistry A.
This journal is © The Royal Society of Chemistry 2020

Ultrafine oxygen-defective iridium oxide nanoclusters for efficient and durable water oxidation at high current densities in acidic media

Zhipeng Yu,‡[ab] Junyuan Xu,‡[a] Yifan Li,‡[c] Bin Wei,[a] Nan Zhang,[a] Yue Li,[ad] Oleksandr Bondarchuk,[a] Hongwei Miao,[a] Ana Araujo,[a] Zhongchang Wang,[a] Joaquim Luis Faria,[b] Yuanyue Liu*[c] and Lifeng Liu*[a]

[a] International Iberian Nanotechnology Laboratory (INL), Avenida Mestre Jose Veiga, 4715-330 Braga, Portugal

[b] Laboratory of Separation and Reaction Engineering – Laboratory of Catalysis and Materials (LSRE-LCM), Faculdade de Engenharia, Universidade do Porto, Rua Dr. Roberto Frias s/n 4200-465 Porto, Portugal

[c] Materials Science & Engineering Programme, University of Texas at Austin, USA

[d] Center of Chemistry, Chemistry Department, University of Minho, Gualtar Campus, 4710-057 Braga, Portugal

‡ These authors contribute equally to this work

* Corresponding author email. yuanyue.liu@austin.utexas.edu (Y. Liu); lifeng.liu@inl.int (L. Liu)

Experimental Procedures

Reagents

All reagents were used as received without further purification. Ti foam was purchased from Xiamen Tmax Battery Equipments Limited. China. Nafion® perfluorinated resin solution (5 wt %) were purchased from Sigma-Aldrich. Potassium hydroxide (KOH), Iridium(III) chloride hydrate ($IrCl_3 \cdot x\, H_2O$) and IrO_2 powders were acquired from Alfa Aesar.

Materials Synthesis

Synthesis of H-Ti foam: The H-Ti foam was prepared using a hydrothermal method similar to that reported previously with some modification.[S1] In a typical procedure, a piece of Ti foam was cleaned by ultra-sonication in acetone, ethanol and deionized (DI) water for 30 min each time, and then dried under vacuum at 70 ^oC. The dried Ti foam (1 × 1 cm^2) was then immersed into 20 mL of 10 M KOH solution in a Teflon-lined stainless steel autoclave. The autoclave was sealed, heated up to 90 ^oC, and maintained at this temperature for 6 h in an oven. After cooling down to room temperature naturally, the obtained H-Ti foam was washed with DI water several times and dried under vacuum at 70 ^oC for further use.[S2]

Oxidization of carbon paper: The oxidation of carbon paper was conducted using a mixed acid solution as described in our previous work with some modification.[S3] Typically, a piece of carbon paper (1 × 1 cm^2) was immersed in a mixed solution of sulfuric acid, nitric acid and water (v(98% H_2SO_4):v(70% HNO_3):v(H_2O) = 1:1:1) at 70 ^oC for 2 h under vigorous magnetic stirring. The obtained carbon paper was washed with DI water several times and dried under vacuum at 70 ^oC for further use.

Synthesis of H-Ti@IrO$_x$: To load IrO$_x$ on H-Ti foam, 89.6 mg of $IrCl_3 \cdot xH_2O$ was firstly added to 3 mL of H_2O, and the solution was sonicated for 1 h to form 100 mM aqueous solution of $IrCl_3$. Then a piece of dried H-Ti foam (1 × 1 cm^2) was soaked in the $IrCl_3$ solution for 30 min to obtain H-Ti@IrCl$_3$. Afterwards, H-Ti@IrCl$_3$ was thermally annealed at 400 ^oC for 30 min in air.[S4,S5] The loading density of IrO$_x$ on H-Ti could be adjusted by repeating the above-mentioned soaking-annealing process, and 1 – 4 repeats gave rise to a loading density of 0.13, 0.25, 0.35, and 0.60 mg cm^{-2} (denoted as H-Ti@IrO$_x$-0.13 mg cm^{-2}, H-Ti@IrO$_x$-0.25 mg cm^{-2}, H-Ti@IrO$_x$-0.35 mg cm^{-2}, and H-Ti@IrO$_x$-0.60 mg cm^{-2}), respectively. According to the electrocatalytic tests, H-Ti@IrO$_x$-0.25 mg cm^{-2} showed the best catalytic performance for OER, and therefore most physicochemical characterization was carried out based on H-Ti@IrO$_x$-0.25 mg cm^{-2} (denoted as H-Ti@IrO$_x$ in the main text for simplicity).

The C@IrO$_x$ and P-Ti@IrO$_x$ control samples were prepared according to the procedures similar to those described above with two soaking-annealing cycles. However, in these cases $IrCl_3$ precursor solution with a lower concentration (25 mM for C@IrO$_x$ and 6.25 mM for P-Ti@IrO$_x$) was used. This led to an IrO$_x$ loading density of 0.24 mg cm^{-2} for C@IrO$_x$ and 0.39 mg cm^{-2} for P-Ti@IrO$_x$.

The IrO$_x$ loading was measured using a high precision micro-balance (Sartorius, readability: 0.001 mg) by subtracting the mass of the catalyst support (H-Ti, P-Ti, or carbon paper) subjected to the annealing treatment under the same conditions as those for preparing the catalysts (H-Ti@IrO$_x$, P-Ti@IrO$_x$ or C@IrO$_x$) from the mass of the final catalysts. Measurements from three batches of samples were carried out and an average value was used to denote the loading mass.

Materials characterization: XRD experiments were conducted on an X'Pert PRO diffractometer (PANalytical) set at 45 kV and 40 mA, using Cu *K*α radiation (λ = 1.541874 Å) and a PIXcel detector. Data were collected with the Bragg–Brentano configuration in the 2θ range of 30 – 100^o at a scan speed of 0.011^o s^{-1}. XPS characterization was carried out on an ESCALAB 250 instrument with Al *K*α X-rays (1486.6 eV). SEM examination was performed on a FEI Quanta 650 FEG microscope equipped with INCA 350 spectrometer (Oxford Instruments) for EDX. TEM, HRTEM and EDX elemental mapping studies were conducted on a probe-corrected transmission electron microscope operating at 200 kV (FEI Themis 60-300). Raman spectroscopy examination was done on a confocal Raman spectrometer (Witec Alpha 300R). The mass loss of Ir and Ti was detected by the inductively coupled plasma – optical emission spectroscopy (ICP–OES, ICPE-9000 spectrometer, Shimadzu) after different time intervals. Electrolyte solution was sampled every 25 h during the stability test, and was filtrated prior to each ICP-OES analysis.

DFT calculations: Density functional theory calculations were performed using Vienna Ab-initio Simulation Package (VASP), with projector augmented wave (PAW) pseudopotential and Perdew–Burke–Ernzerhof (PBE) exchange-correlation functional.[S6-S8] A kinetic energy cut-off of 450 eV was adopted for the plane-wave expansion, and 5×5×1 K-point mesh was used. All structures were fully relaxed until the final energy and force on each atom were less than 10^{-5} eV and 0.02 eV $Å^{-1}$, respectively. Vacuum space above the IrO_2 (110) surface was kept to >15 Å. The overall OER likely proceeds through two pathways, namely the conventional adsorbate evolution mechanism (AEM) and the lattice oxygen mechanism (LOM), both including the following reaction steps:[S9]

AEM – adsorbate evolution mechanism	LOM – lattice oxygen mechanism
$H_2O\ (aq) + {}^* \rightarrow OH^* + e^- + H^+$ (1)	$H_2O\ (aq) + {}^* \rightarrow OH^* + e^- + H^+$ (1’)
$OH^* \rightarrow O^* + e^- + H^+$ (2)	$OH^* \rightarrow O^* + e^- + H^+$ (2’)
$O^* + H_2O\ (aq) \rightarrow OOH^* + e^- + H^+$ (3)	$O^* + O_{lat} \rightarrow O_2 \uparrow + V_o$ (3’)
$OOH^* \rightarrow OO^* + e^- + H^+$ (4)	$V_o + H_2O\ (aq) \rightarrow H^* + e^- + H^+$ (4’)
$OO^* \rightarrow {}^* + O_2 \uparrow$ (5)	$H^* \rightarrow {}^* + e^- + H^+$ (5’)

where *, O_{lat}, V_o represent the Ir active site, lattice oxygen and lattice oxygen vacancy, respectively, and OH^*, O^*, OOH^*, OO^* and $H^*$are the intermediates absorbed on the active sites during the OER. The adsorption energy was calculated according to the formula $E_{ad} = E_{sys} – E_{sur} – E_{spe}$, in which E_{ad}, E_{sys}, E_{sur} and E_{spe} denote the adsorption energy, the energy of adsorption system, the energy of clean surface and the energy of isolated adsorption species. The Gibbs free energy changes of these steps were calculated as follows:[S10]

AEM – adsorbate evolution mechanism	LOM – lattice oxygen mechanism
$\Delta G_1 = G(OH^*) - G(^*) - G(H_2O) + \frac{1}{2} G(H_2(g)) - \lvert e \rvert U$ (6)	$\Delta G_1 = G(OH^*) - G(^*) - G(H_2O) + \frac{1}{2} G(H_2(g)) - \lvert e \rvert U$ (6’)
$\Delta G_2 = G(O^*) - G(OH^*) + \frac{1}{2} G(H_2(g)) - \lvert e \rvert U$ (7)	$\Delta G_2 = G(O^*) - G(OH^*) + \frac{1}{2} G(H_2(g)) - \lvert e \rvert U$ (7’)
$\Delta G_3 = G(OOH^*) - G(O^*) - G(H_2O) + \frac{1}{2} G(H_2(g)) - \lvert e \rvert U$ (8)	$\Delta G_3 = G(O_2(g)) + G(V_o) - G(O^*) - G(O_{lat})$ (8’)
$\Delta G_4 = G(OO^*) - G(OOH^*) + \frac{1}{2} G(H_2(g)) - \lvert e \rvert U$ (9)	$\Delta G_4 = G(H^*) - G(V_o) - G(H_2O) + \frac{1}{2} G(H_2(g)) - \lvert e \rvert U$ (9’)
$\Delta G_5 = G(^*) + G(O_2(g)) - G(OO^*)$ (10)	$\Delta G_5 = G(^*) - G(H^*) + \frac{1}{2} G(H_2(g)) - \lvert e \rvert U$ (10’)

Electrode preparation and electrocatalytic tests: All the electrocatalytic tests were carried out in a three electrode configuration at room temperature using a Biologic VMP-3 potentiostat/galvanostat. The as-fabricated of H-Ti@IrO$_x$, C@IrO$_x$ or P-Ti@IrO$_x$ (1 × 1 cm^2) was directly used as the working electrode. A Pt wire and a saturated calomel electrode (SCE) were utilized as the counter and reference electrodes, respectively. The SCE reference was calibrated prior to each measurement in Ar/H_2-saturated 0.5 M H_2SO_4 solution using a clean Pt wire as the working electrode. Unless otherwise stated, all potentials are reported versus RHE by converting the measured potentials according to the following equation:

$$E_{\mathrm{RHE}} = E_{\mathrm{SCE}} + 0.059 \times \mathrm{pH} + 0.241 \quad (11)$$

For commercial IrO_2 powders, the catalyst ink was prepared by ultrasonically dispersing 10 mg of IrO_2 into 950 μL of ethanol containing 50 μL of Nafion® solution. 30 μL of the catalyst ink was loaded on a piece of glassy carbon (GC) substrate (0.78 cm^2), leading to a catalyst loading density of 0.39 mg cm^{-2}. The electrode was then dried at room temperature naturally in air.

The apparent OER activity was appraised using cyclic voltammetry (CV) at a scan rate of 5 mV s^{-1}, and an *iR*-correction (85%) was applied to compensate for the voltage drop between the reference and working electrodes, which was measured by a single-point high-frequency impedance measurement. The reduction branches of the CV curves were used to compare the performance of all catalysts.

The ECSAs were estimated from the electrochemical double-layer capacitance of the catalytic surface. The double-layer capacitance (C_{dl}) of catalysts was derived by performing CV in the potential range of 0.66 to 1.06 V *vs* RHE (non-Faradaic potential range) at different scan rates (v) of 10, 20, 30, 40, 50, 60, 70, 80, 90 and 100 mV s^{-1}, followed by extracting the slope from the resulting $|j_a-j_c|/2$ *vs* v plots (j_a and j_c represent the anodic and cathodic current at 0.86 V *vs* RHE). The ECSA can be then calculated by dividing the measured C_{dl} by the capacitance of a model catalyst over a unit surface area (0.04 mF cm_{geo}^{-2} for metal oxide).[S11]

$$\mathrm{ECSA} = C_{\mathrm{dl}} / 0.04\ \mathrm{mF\ cm^{-2}} \qquad (12)$$

EIS measurements were carried out at 1.51 V *vs* RHE in the frequency range of 10^5 to 0.01 Hz with a 10 mV sinusoidal perturbation. The stability of catalysts was assessed at a constant current density of 200 mA $\mathrm{cm^{-2}}$ using chronopotentiometry (CP).

Supplementary figures

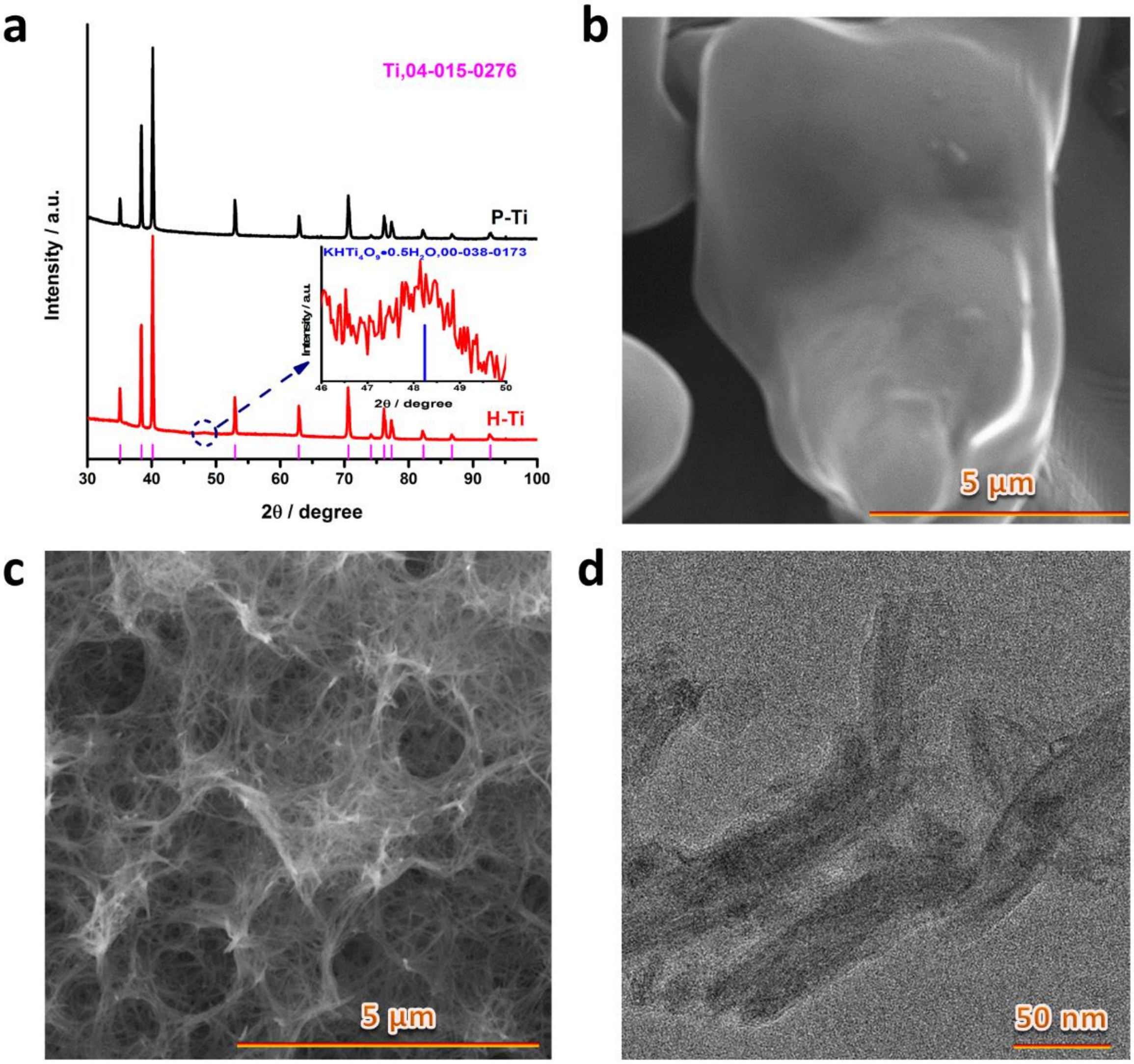

Fig. S1 (a) XRD patterns of P-Ti foam and H-Ti foam. SEM images of (b) P-Ti foam and (c) H-Ti foam. (d) TEM image of H-Ti foam. PHT nanowires were obtained upon the hydrothermal treatment.

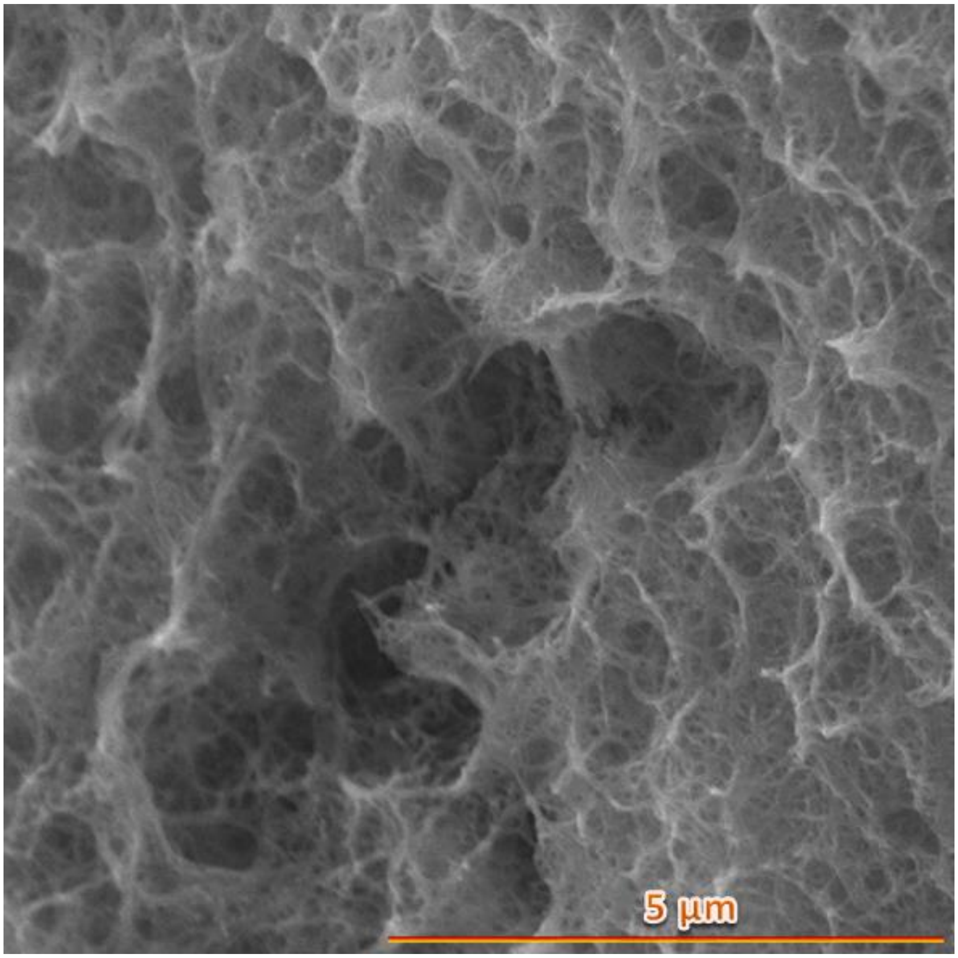

Fig. S2 SEM image of H-Ti@IrO_x catalysts.

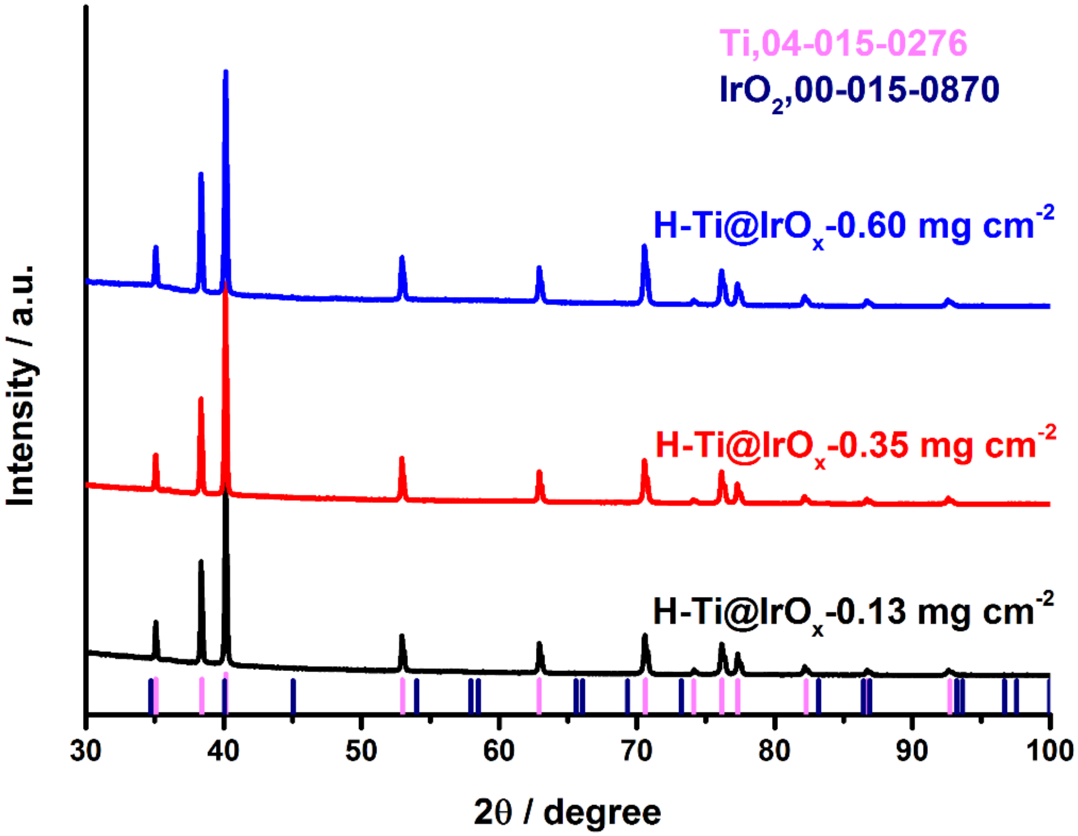

Fig. S3 XRD patterns of H-Ti@IrO_x-0.13 mg cm^{-2}, H-Ti@IrO_x-0.35 mg cm^{-2} and H-Ti@IrO_x-0.60 mg cm^{-2}.

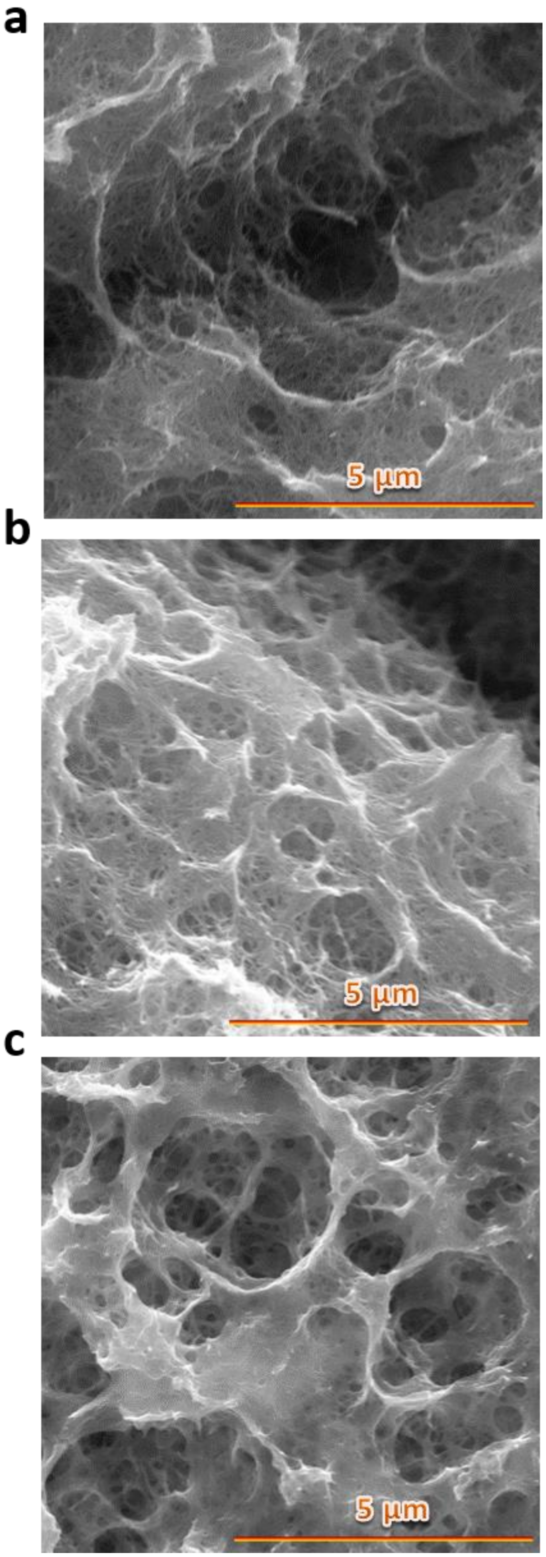

Fig. S4 SEM images of (a) H-Ti@IrO$_x$-0.13 mg cm^{-2}, (b) H-Ti@IrO$_x$-0.35 mg cm^{-2} and (c) H-Ti@IrO$_x$-0.60 mg cm^{-2}.

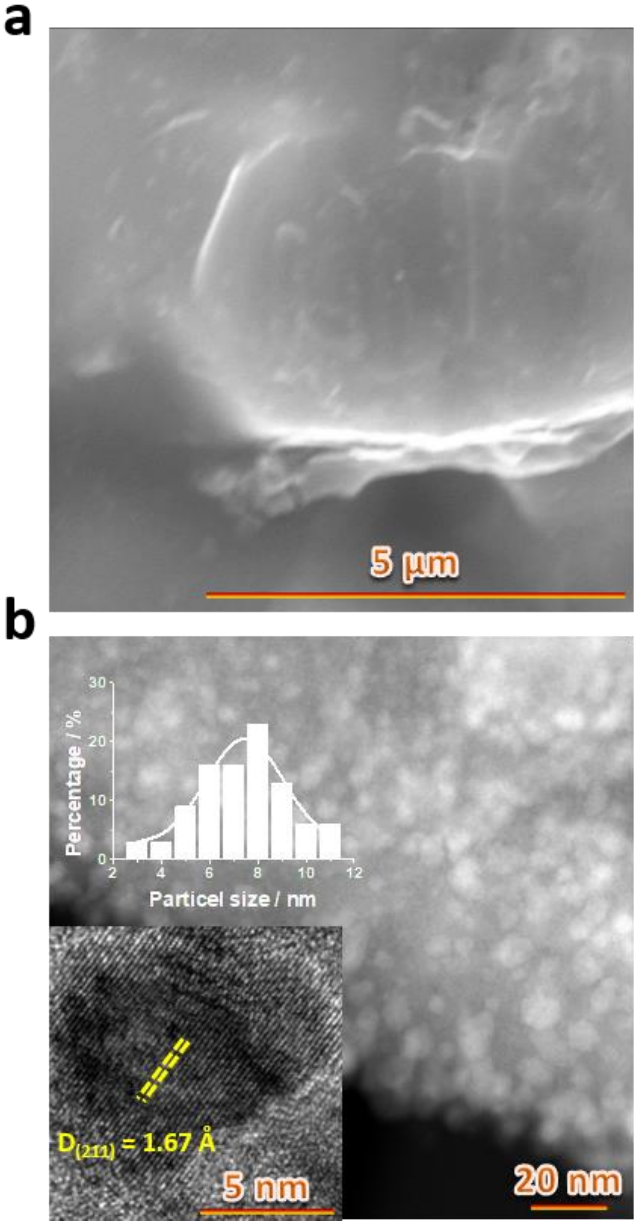

Fig. S5 Morphology and microstructure characterization of P-Ti@IrO_x catalyst. (a) SEM image. (b) HAADF-STEM image. Bottom left inset is the HRTEM image of individual IrO_x nanoclusters, and the marked lattice fringe of 0.167 nm corresponds to the (211) crystal planes of tetragonal IrO_2 (ICDD No. 00-015-0870). Upper left inset is a histogram illustrating the size distribution of IrO_x nanoclusters.

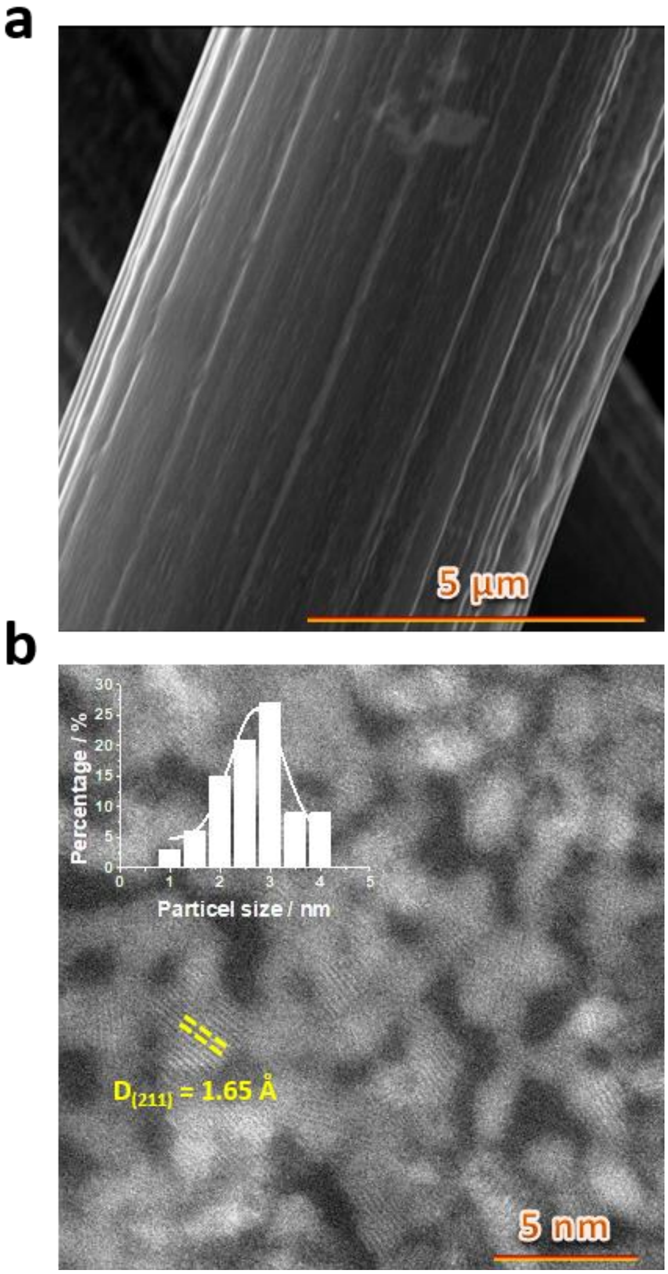

Fig. S6 Morphology and microstructure characterization of C@IrO$_x$. (a) SEM image. (b) HAADF-STEM image. The marked lattice fringe of 0.165 nm corresponds to the (211) crystal planes of tetragonal IrO$_2$ (ICDD No. 00-015-0870). Inset: histogram illustrating the size distribution of ligaments.

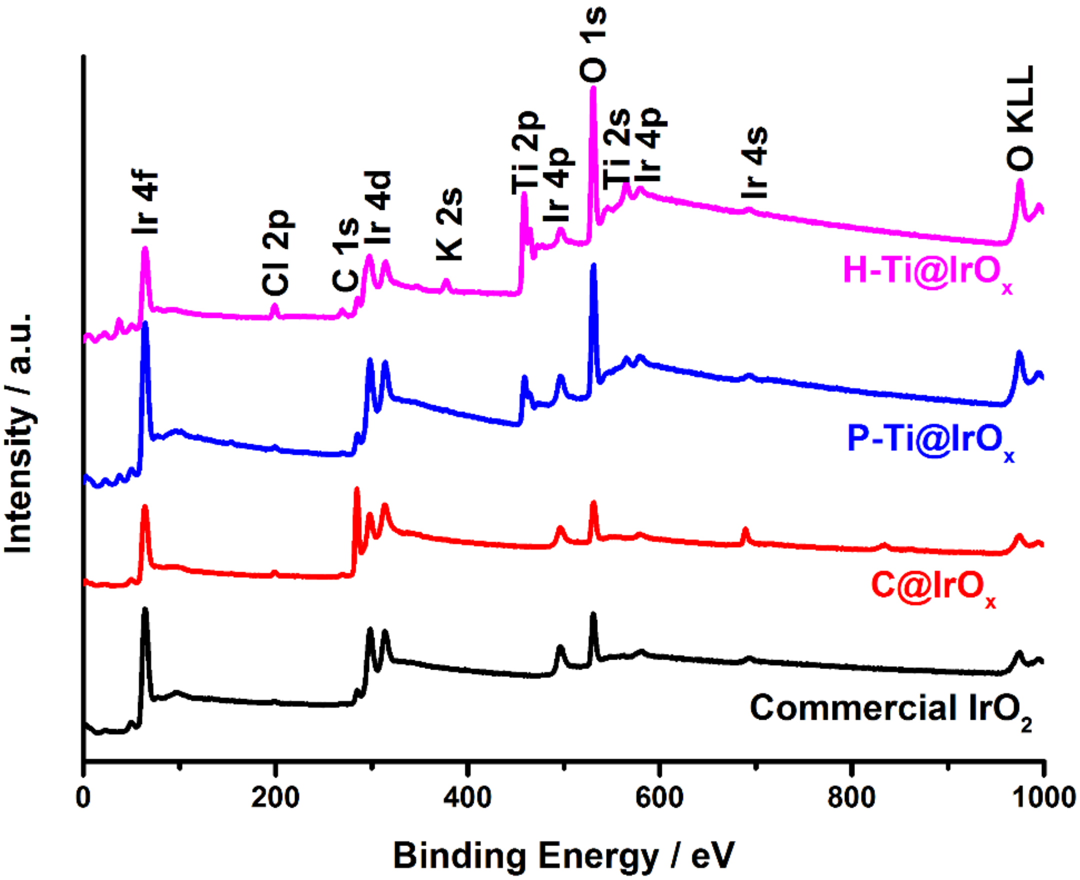

Fig. S7 XPS survey spectra of H-Ti@IrO$_x$, P-Ti@IrO$_x$, C@IrO$_x$, and commercial IrO$_2$ catalysts.

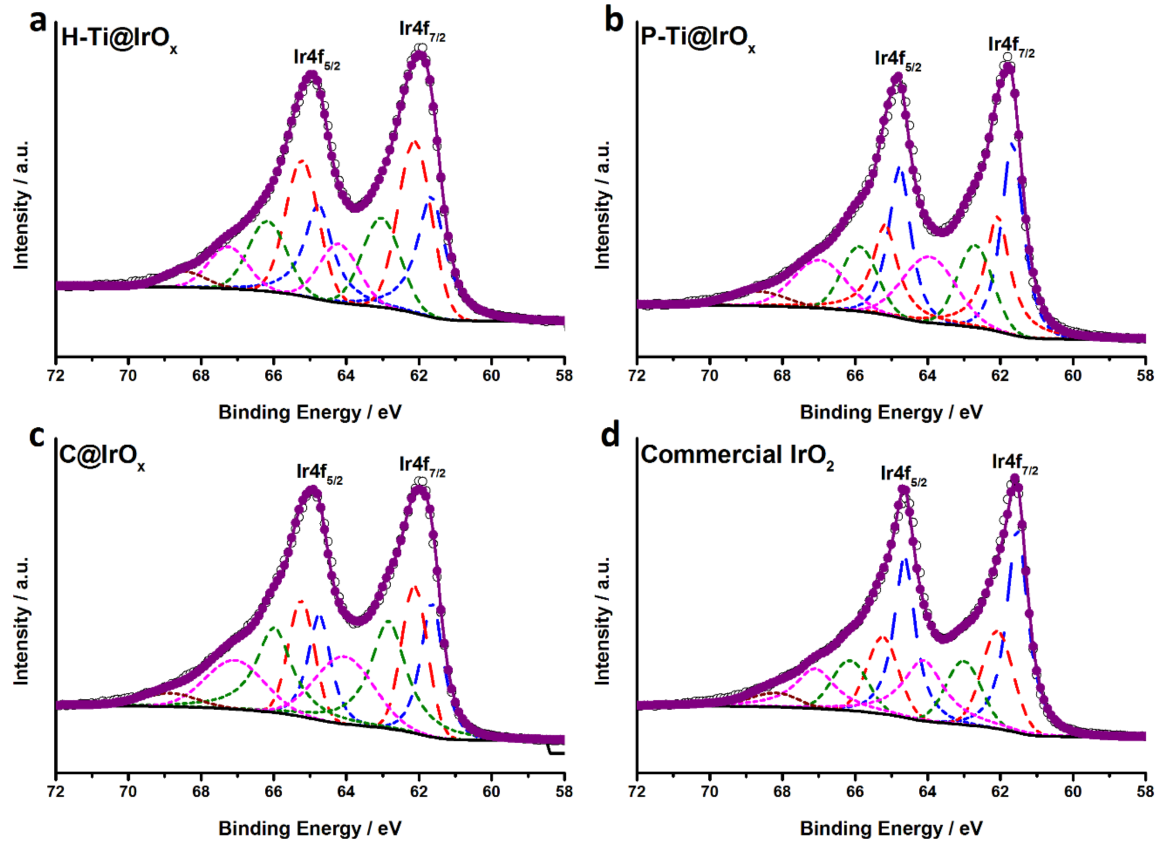

Fig. S8 Ir 4f XPS spectrum of (a) H-Ti@IrO$_x$, (b) P-Ti@IrO$_x$, (c) C@IrO$_x$ and (d) commercial IrO$_2$ catalysts. Blue and red curves represent Ir^{IV} and Ir^{III}, respectively; olive, wine and orange curves represent Ir^{IV} satellite 1, satellite 2 and Ir^{III} satellite, respectively.

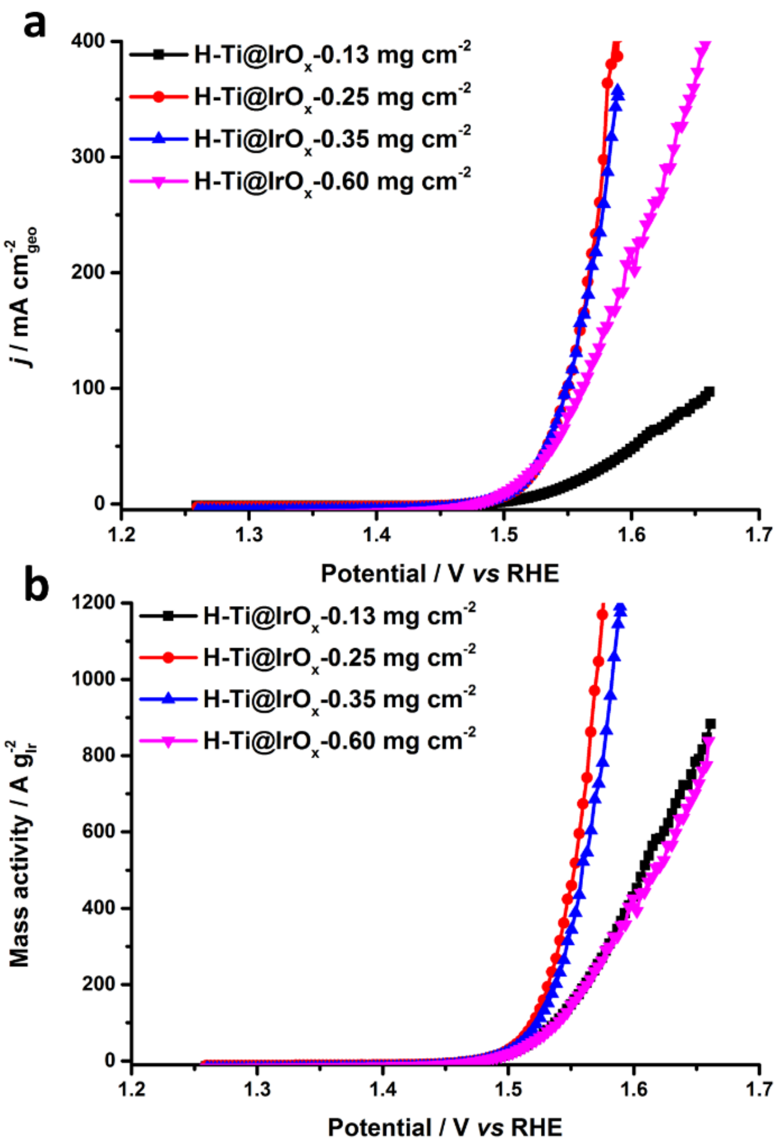

Fig. S9 (a) *iR*-corrected polarization curves and (b) mass activity of H-Ti@IrO$_x$ with different IrO$_x$ loading densities, recorded at a scan rates of 5 mV s^{-1}. The H-Ti@IrO$_x$-0.25 mg cm^{-2} (denoted as H-Ti@IrO$_x$ in the main text for simplicity) shows the best apparent and mass activities and therefore was used in further investigation and the comparison with other control catalysts.

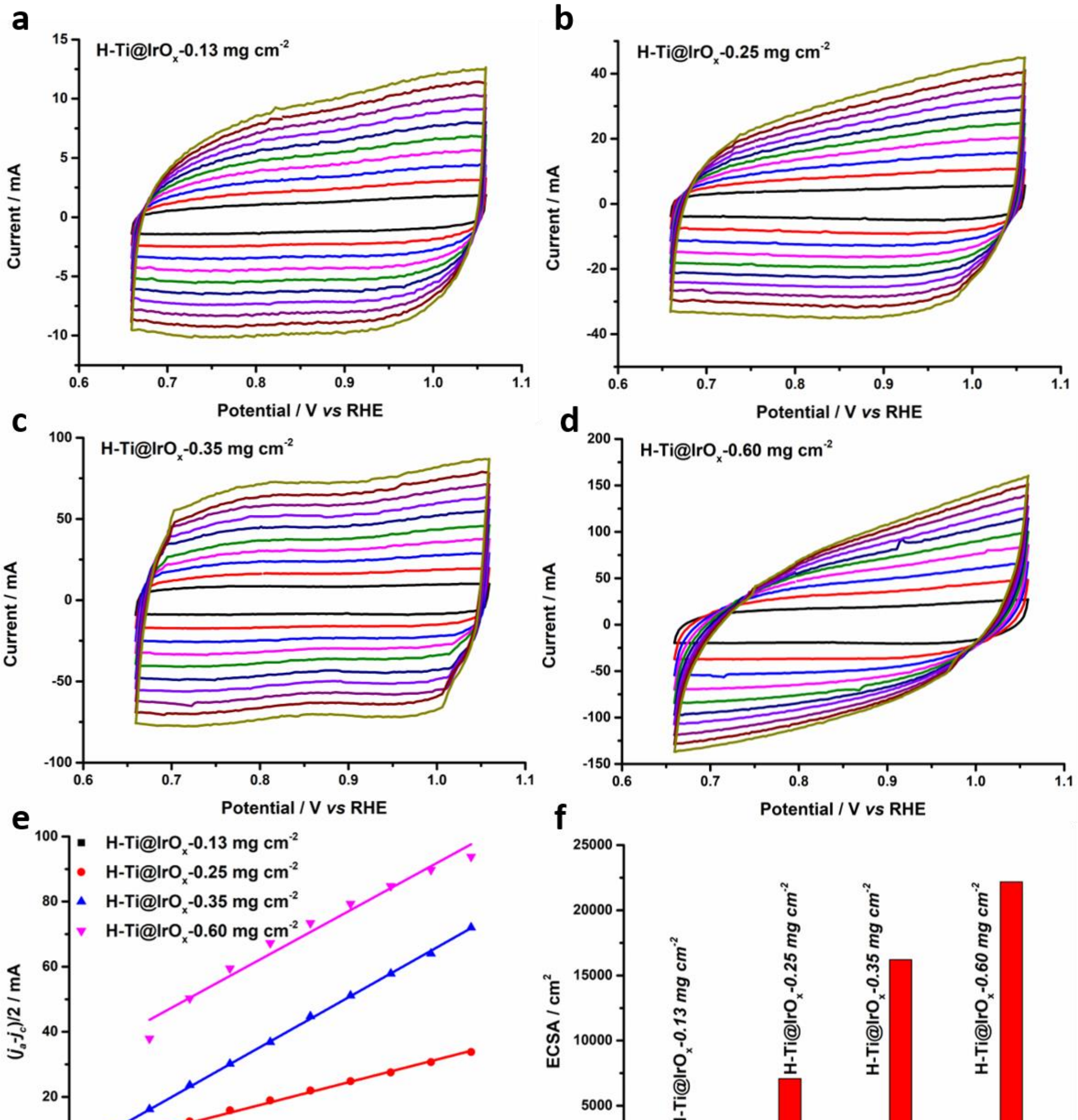

Fig. S10 Electrochemical CV curves of (a) H-Ti@IrO$_x$-0.13 mg cm^{-2}, (b) H-Ti@IrO$_x$-0.25 mg cm^{-2}, (c) H-Ti@IrO$_x$-0.35 mg cm^{-2} and (d) H-Ti@IrO$_x$-0.60 mg cm^{-2}, recorded at different scan rates of 10, 20, 30, 40, 50, 60, 70, 80, 90 and 100 mV s^{-1}. (e) Plots of the capacitive currents as a function of the scan rate for all the catalysts. (f) ECSA of all the catalysts.

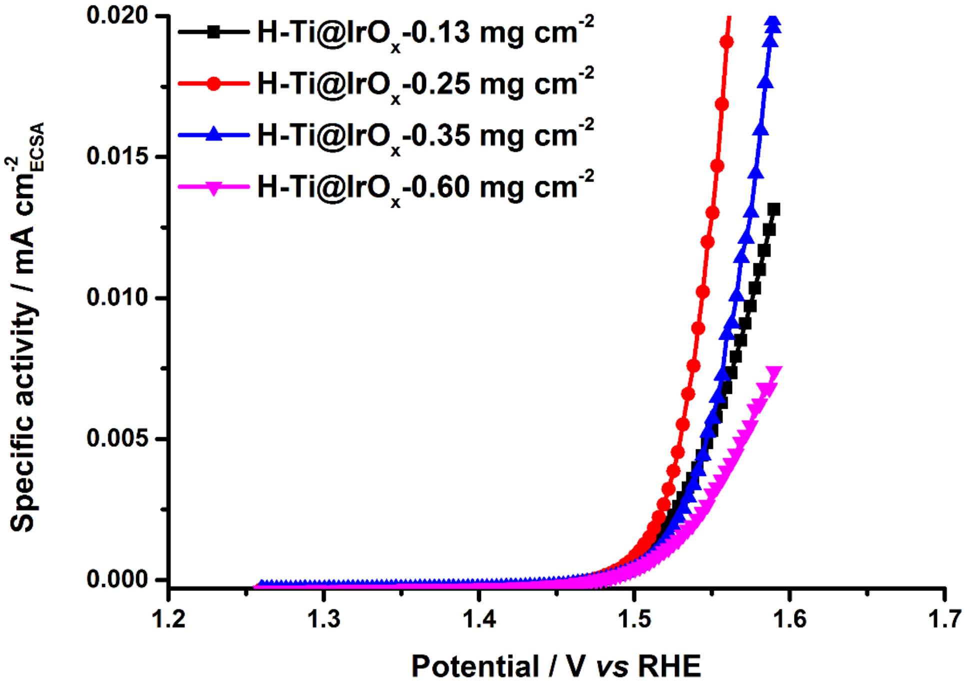

Fig. S11 Specific activity H-Ti@IrO$_x$ with different IrO$_x$ loading densities, recorded at a scan rates of 5 mV s^{-1}.

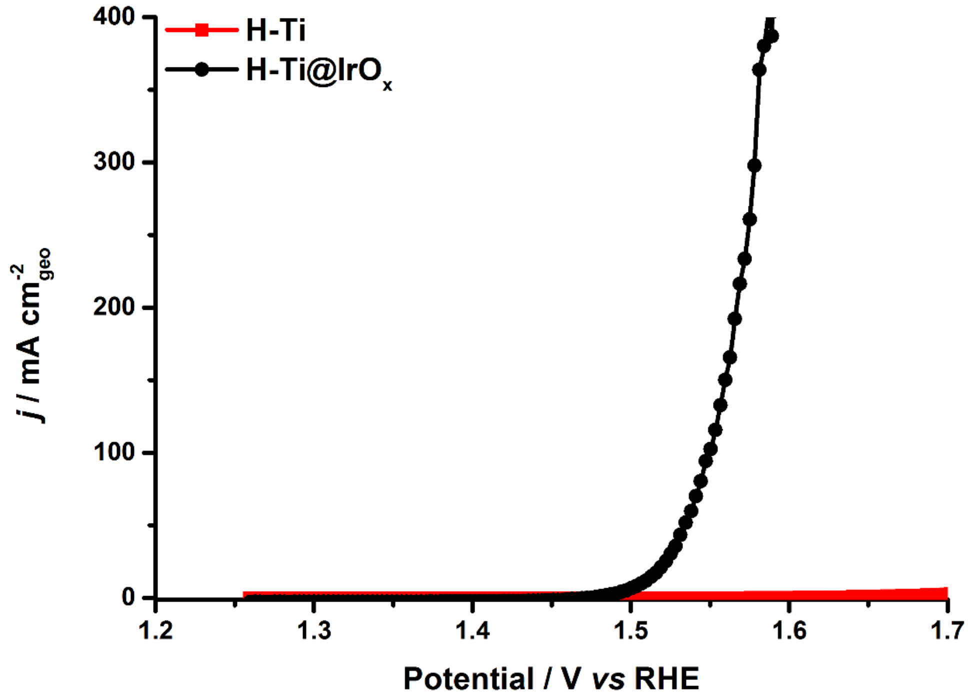

Fig. S12 *iR*-corrected polarization curve of the porous H-Ti foam after the annealing process, recorded in 0.5 M H_2SO_4 at a scan rate of 5 mV s^{-1}.

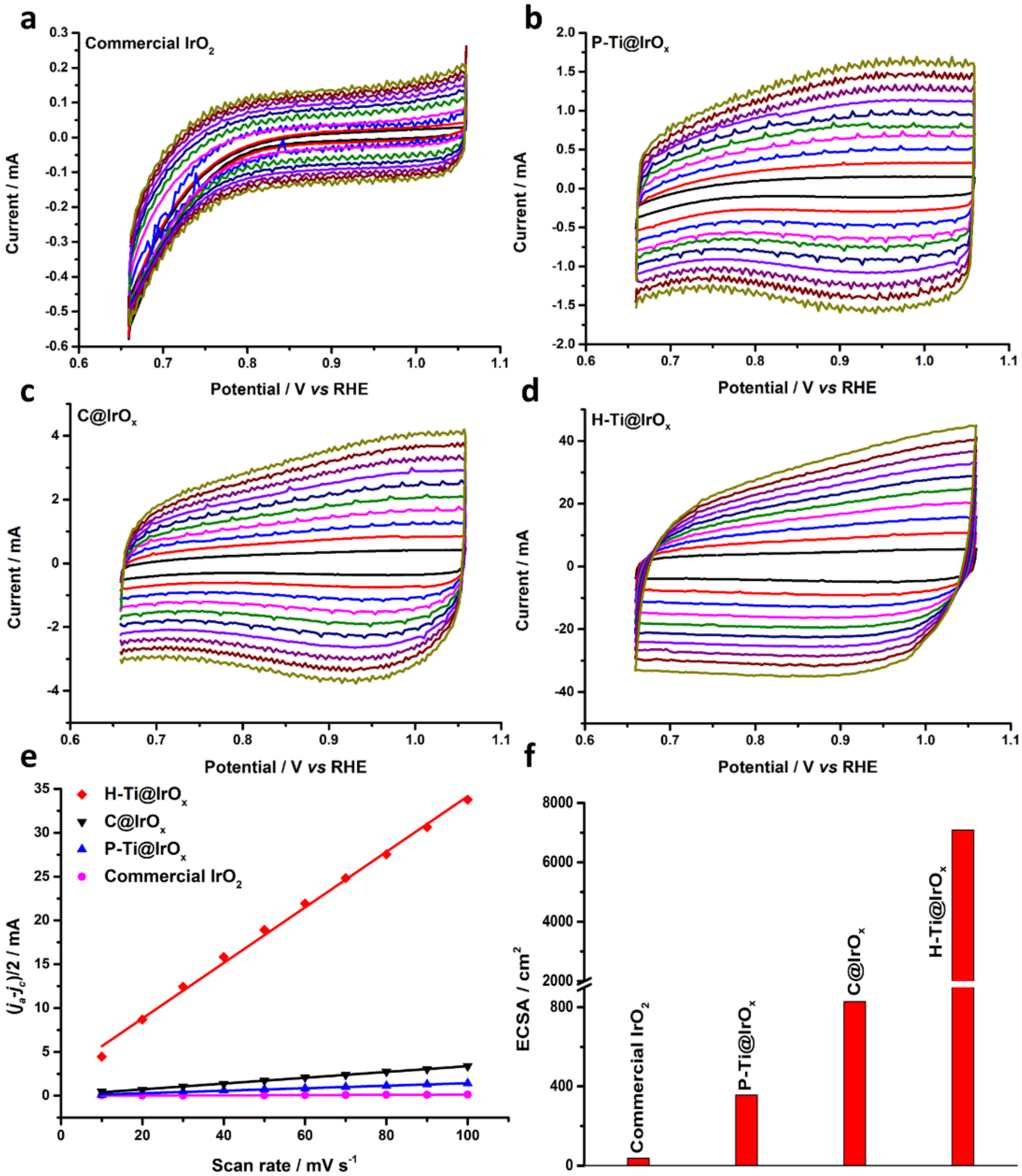

Fig. S13 Electrochemical CV curves of (a) commercial IrO_2, (b) P-Ti@IrO_x, (c) C@IrO_x and (d) H-Ti@IrO_x, recorded at different scan rates of 10, 20, 30, 40, 50, 60, 70, 80, 90 and 100 mV s^{-1}. (e) Plots of the capacitive currents as a function of the scan rate for all the catalysts. (f) ECSA of all the catalysts.

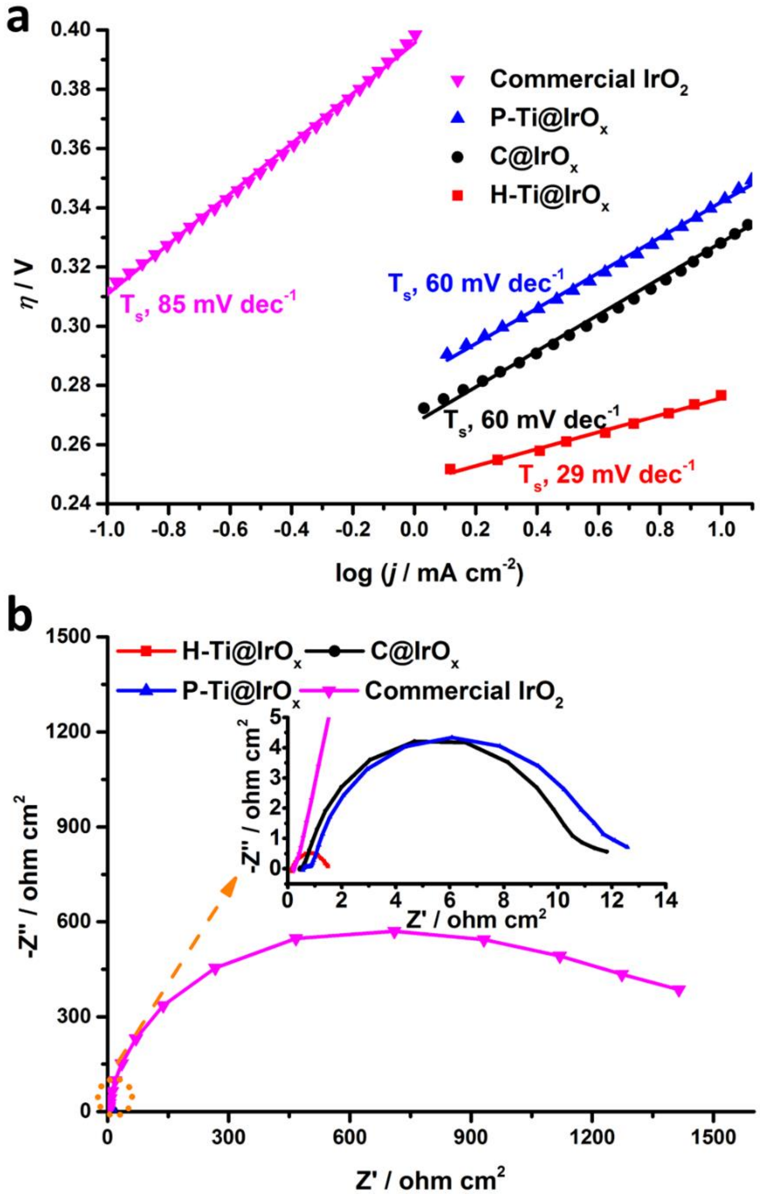

Fig. S14 (a) Tafel plots and (b) Nyquist plots measured at 1.51 V *vs* RHE of all catalysts.

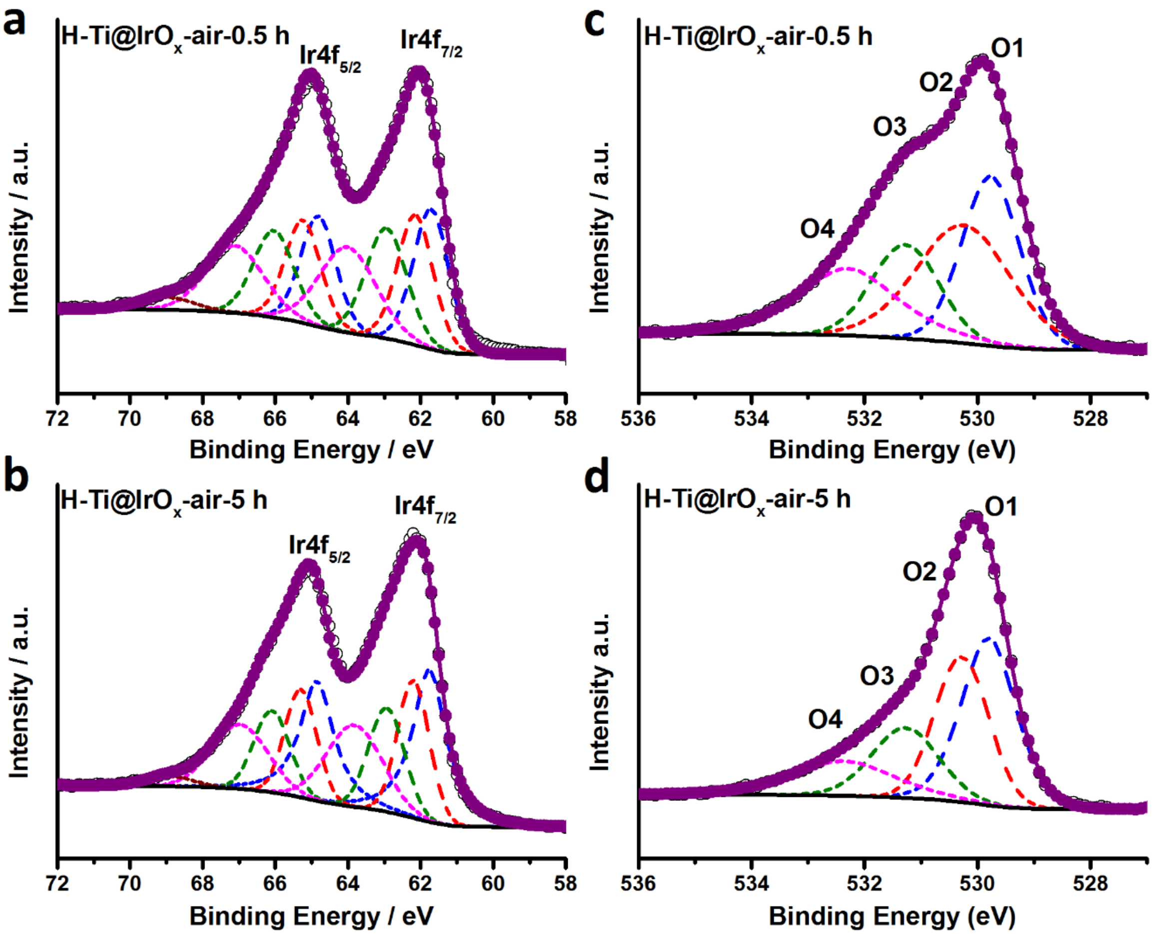

Fig. S15 High resolution (a, b) Ir 4f and (c, d) O 1s spectra of H-Ti@IrO$_x$-air-0.5 h and H-Ti@IrO$_x$-air-5 h. (Blue and red curves represent Ir^{IV} and Ir^{III}, respectively; olive, wine and orange curves represent Ir^{IV} satellite 1, satellite 2 and Ir^{III} satellite, respectively.)

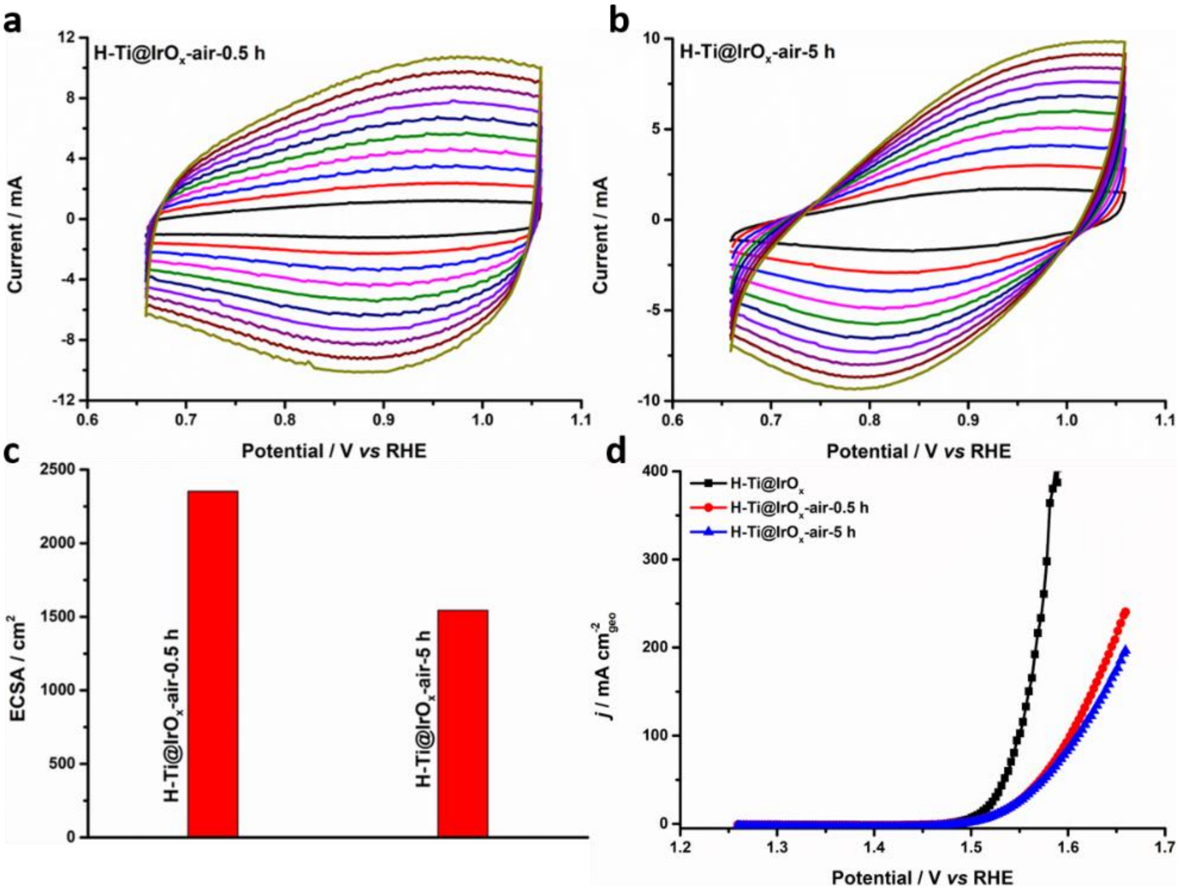

Fig. S16 Electrochemical CV curves of (a) H-Ti@IrO$_x$-air-0.5 h and (b) H-Ti@IrO$_x$-air-5 h, recorded at different scan rates of 10, 20, 30, 40, 50, 60, 70, 80, 90 and 100 mV s^{-1} in the non-Faradaic potential region. (c) ECSA of H-Ti@IrO$_x$-air-0.5 h and H-Ti@IrO$_x$-air-5 h. (d) *iR*-corrected polarization curves of H-Ti@IrO$_x$, H-Ti@IrO$_x$-air-0.5 h and H-Ti@IrO$_x$-air-5 h, recorded at a scan rates of 5 mV s^{-1}.

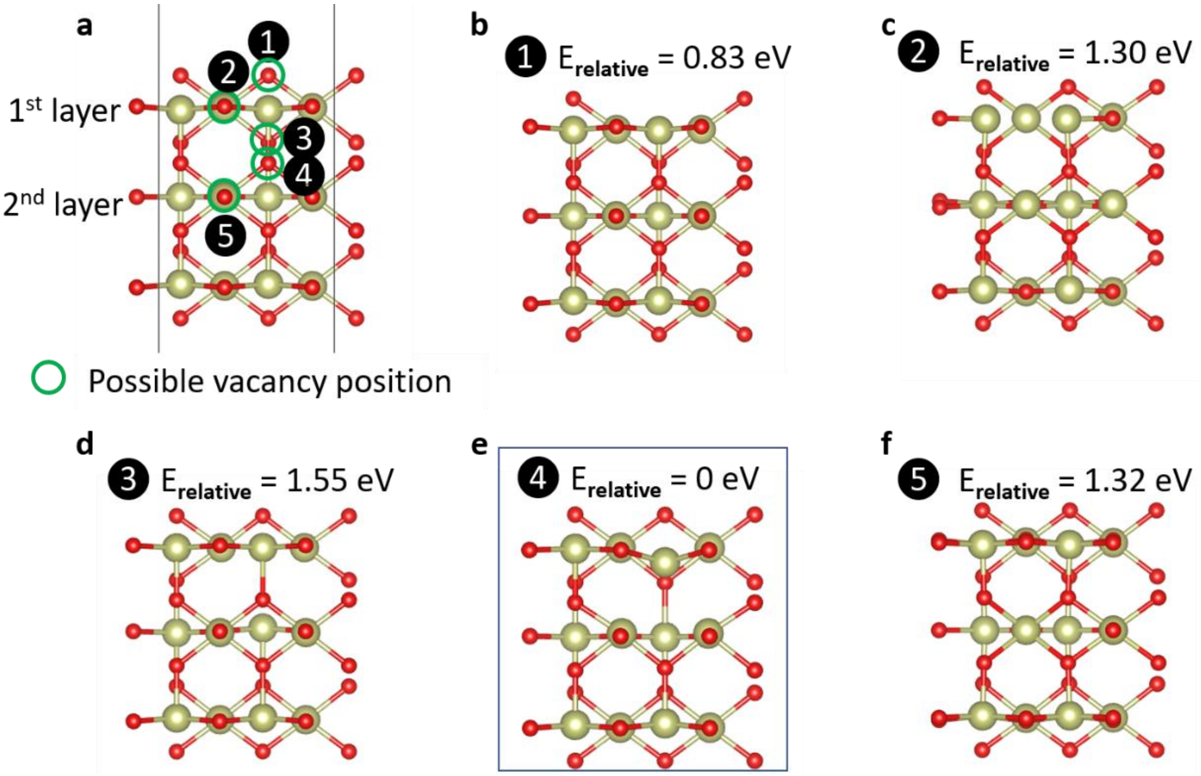

Fig. S17 (a) The five possible oxygen-defective sites introduced on the (110) surface of mono-IrO$_x$, as indicated by green circles. Yellow and red spheres represent Ir and O atoms, respectively. (b-f) mono-IrO$_x$ with an oxygen-defective site at different sites and the relative energy of different models. The relative energy is the difference between the energy of the current structure and the energy of the optimal structure (configuration 4).

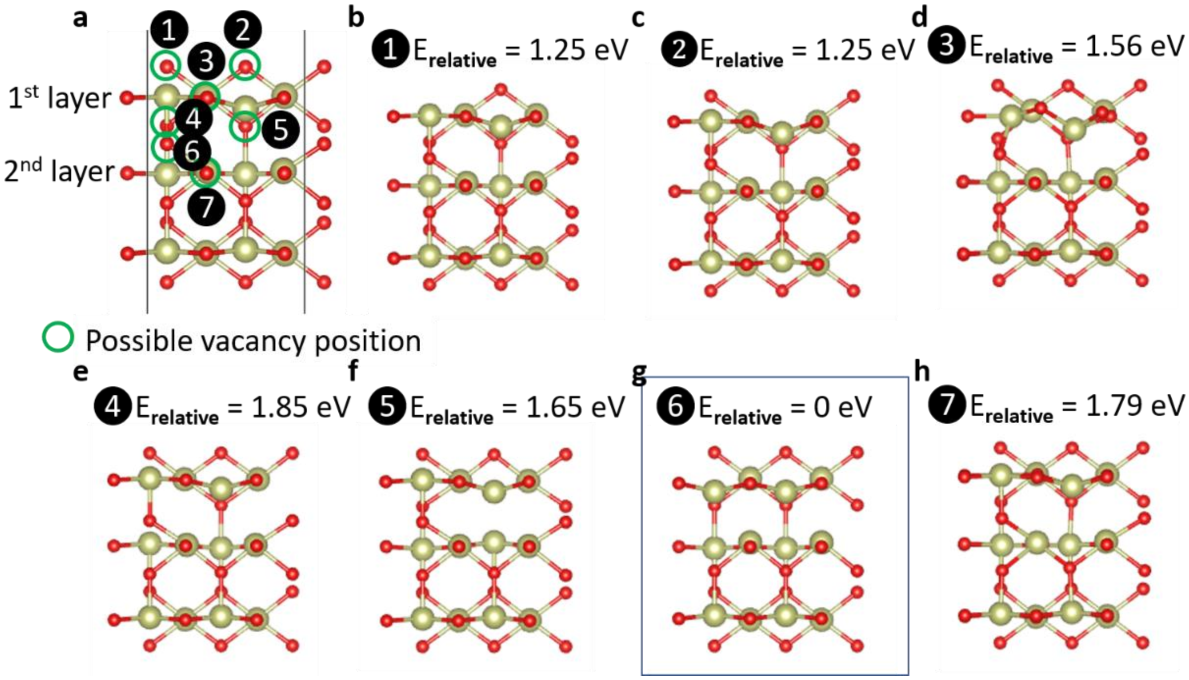

Fig. S18 (a) The seven possible oxygen-defective sites introduced on the (110) surface of bi-IrO_x, as indicated by green circles. Yellow and red spheres represent Ir and O atoms, respectively. (b-h) bi-IrO_x with two oxygen-defective sites at different sites and the relative energy of different models. The relative energy is the difference between the energy of the current structure and the energy of the optimal structure (configuration 6).

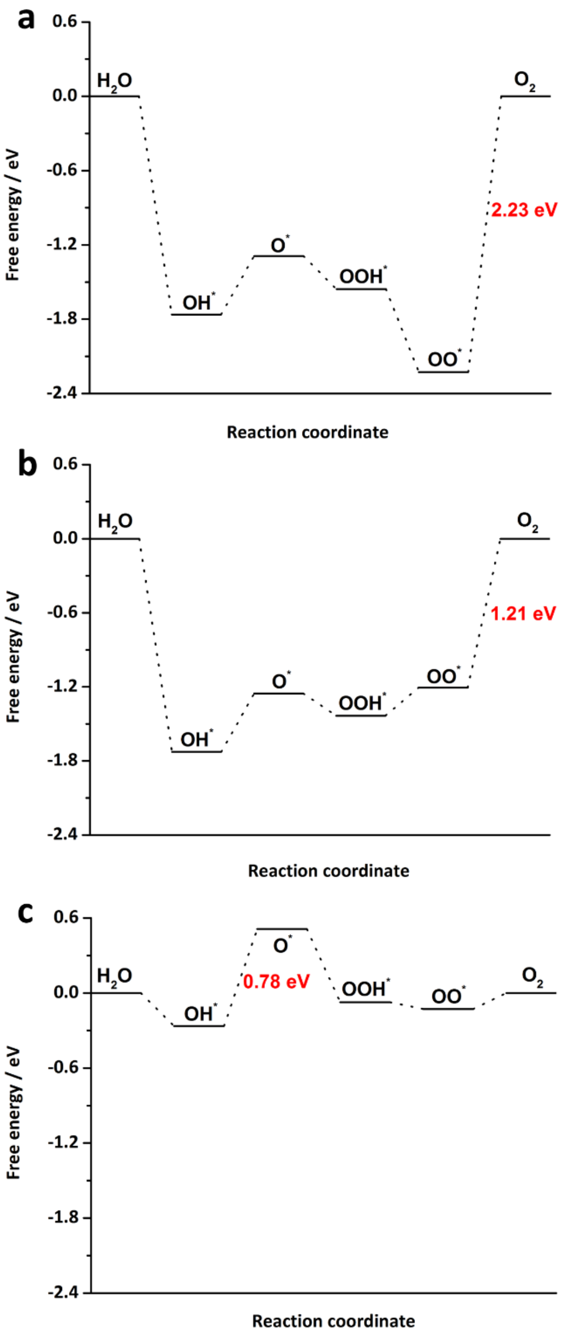

Fig. S19 Gibbs free-energy diagrams for the OER on (a) p-IrO$_2$, (b) mono-IrO$_x$ and (c) bi-IrO$_x$ calculated at U = 1.23 V based on the adsorbate evolution mechanism (AEM).

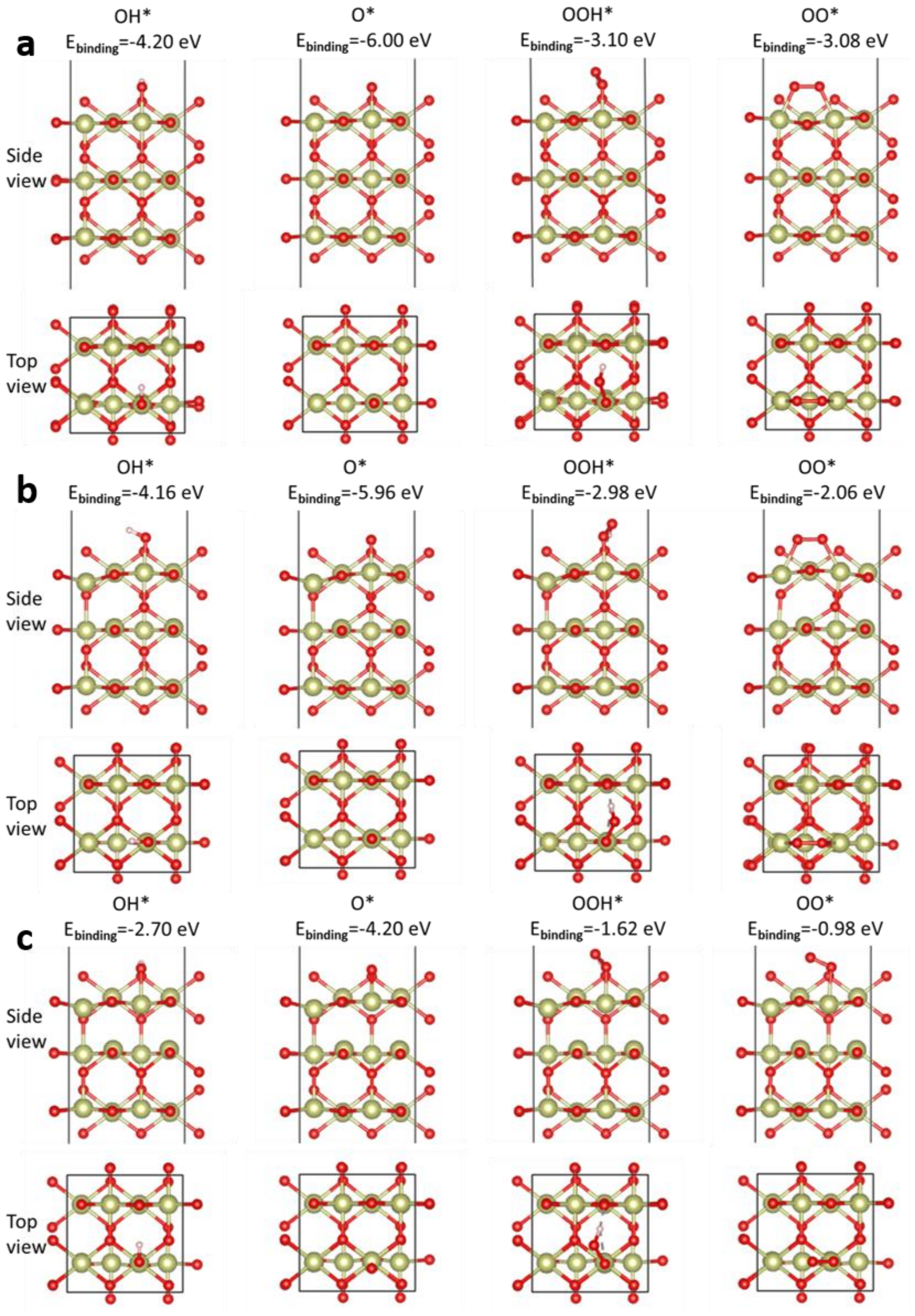

Fig. S20 Optimized geometry of adsorption structure of OH, O, OOH and OO intermediates with the corresponding binding energy on (a) p-IrO_2, (b) mono-IrO_x and (c) bi-IrO_x. Yellow, red and white spheres represent Ir, O and H atoms, respectively.

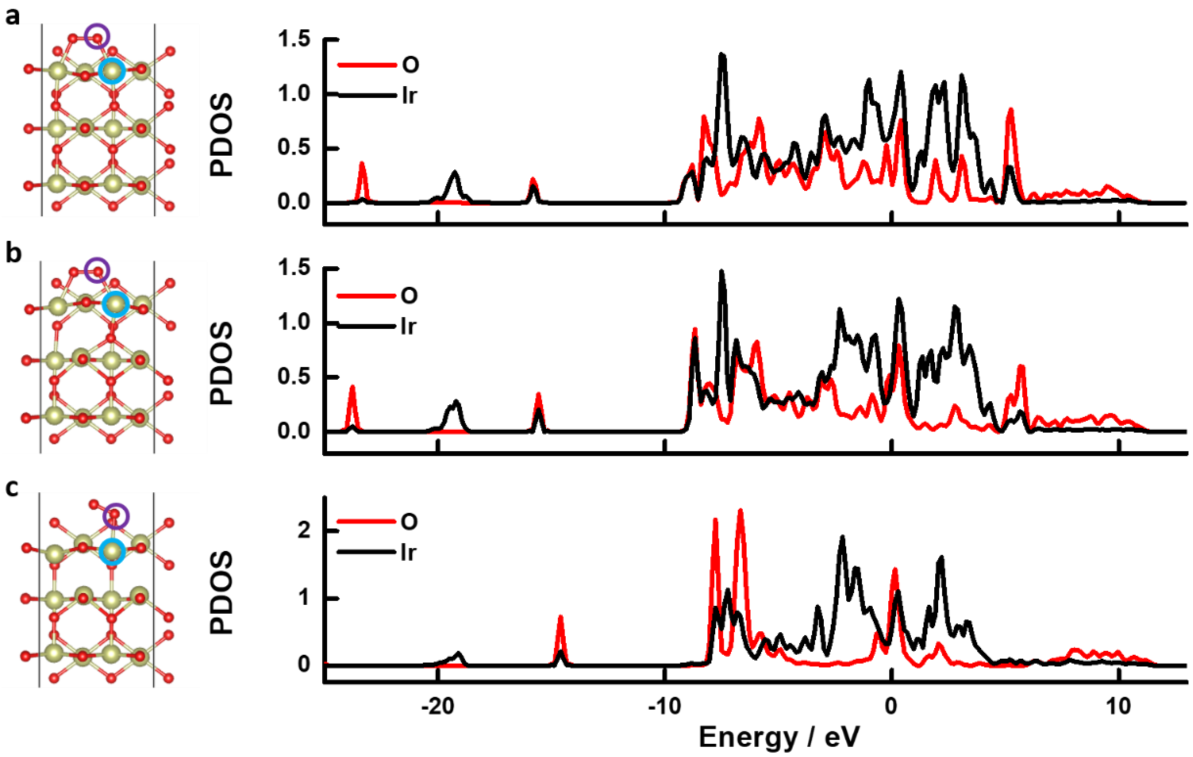

Fig. S21 Calculated PDOS of (a) p-IrO_2, (b) mono-IrO_x and (c) bi-IrO_x after oxygen atoms adsorption. The yellow and red spheres represent Ir and O atoms in all models. The active site and adsorbed oxygen atoms on the active site are labelled by light blue and violet circles, respectively, in the each calculation model.

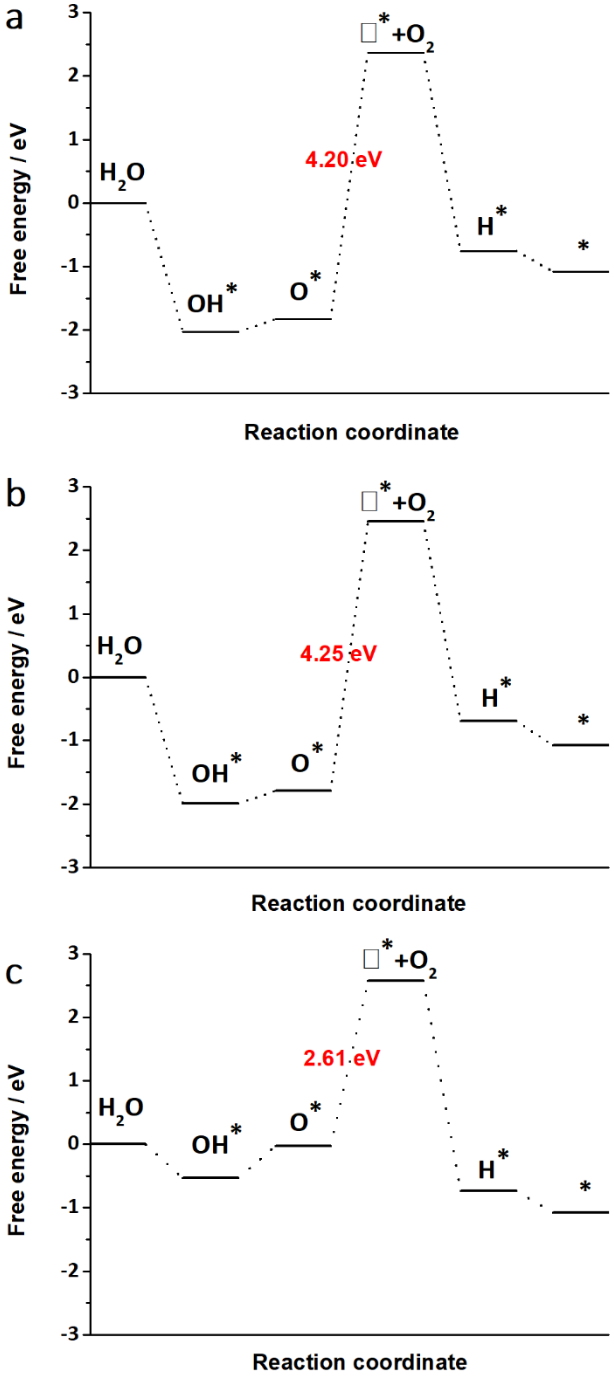

Fig. S22 Gibbs free-energy diagrams for the OER on (a) p-IrO$_2$, (b) mono-IrO$_x$ and (c) bi-IrO$_x$ calculated at U = 1.50 V based on the lattice oxygen mechanism (LOM).

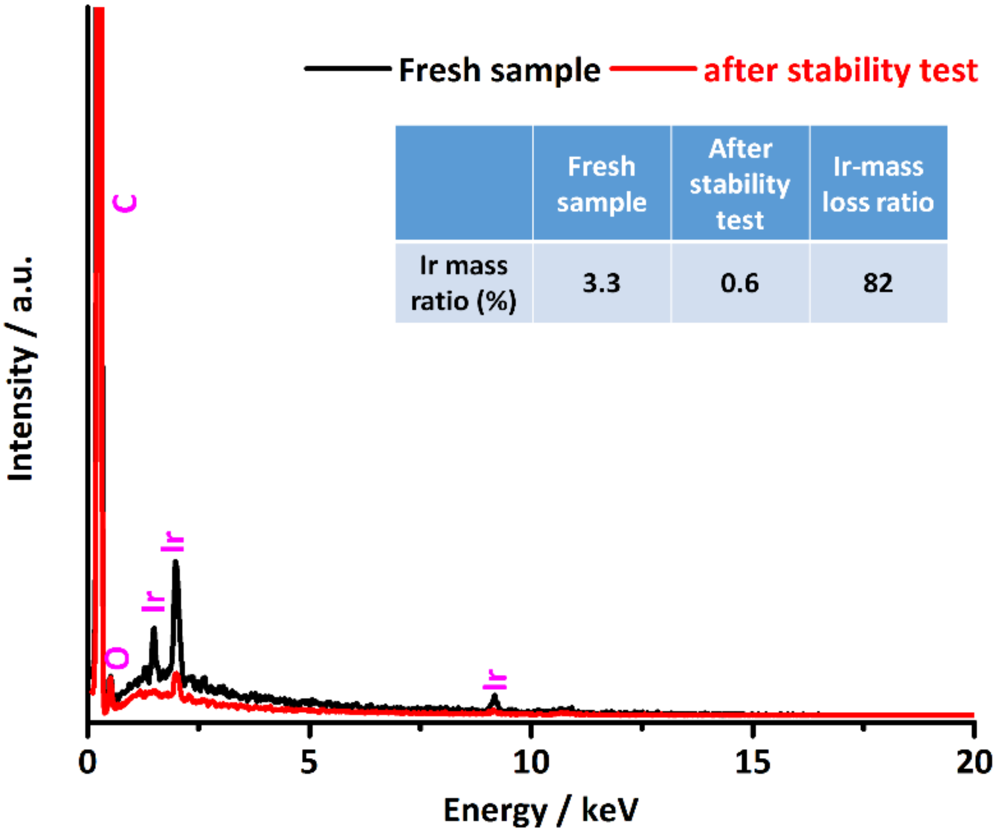

	Fresh sample	After stability test	Ir-mass loss ratio
Ir mass ratio (%)	3.3	0.6	82

Fig. S23 EDX spectra of C@IrO$_x$ before and after the stability test at 200 mA cm^{-2} for 1.5 h, showing that ca. 82 % of initial IrO$_x$ has lost during the stability test.

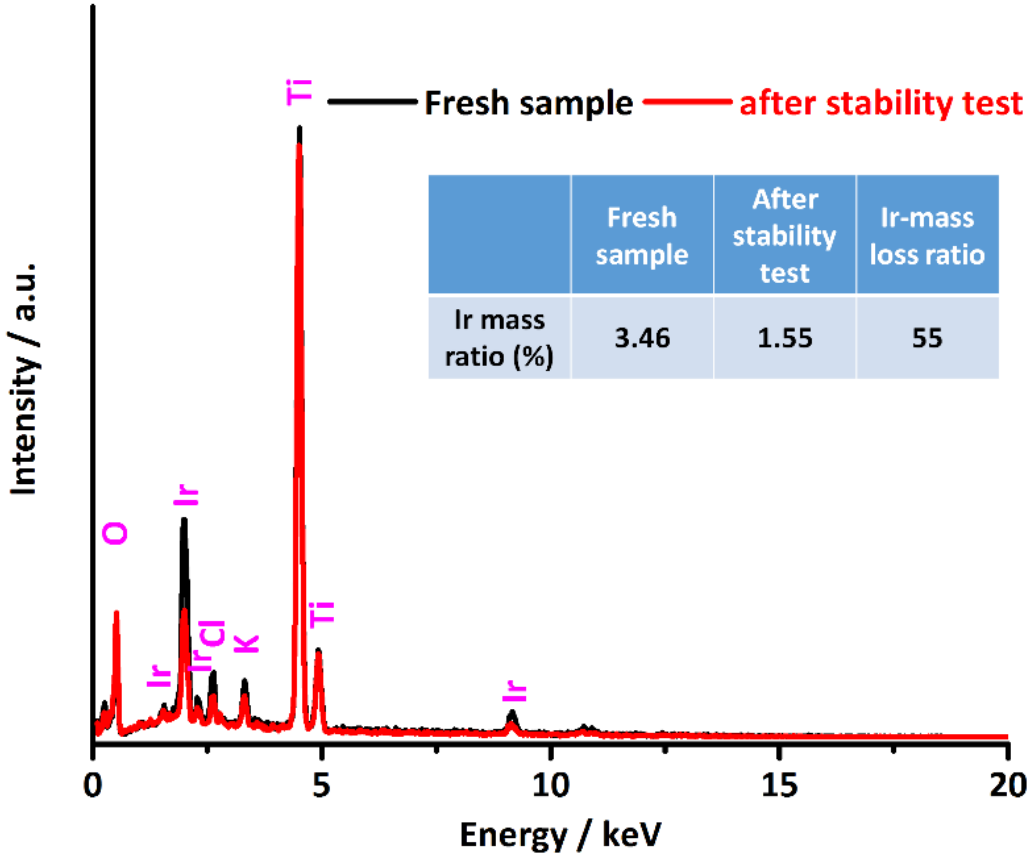

	Fresh sample	After stability test	Ir-mass loss ratio
Ir mass ratio (%)	3.46	1.55	55

Fig. S24 EDX spectra of P-Ti@IrO_x before and after the extended stability test at 200 mA cm^{-2} for 60 h, showing that ca. 55 % of initial IrO_x has lost during the stability test.

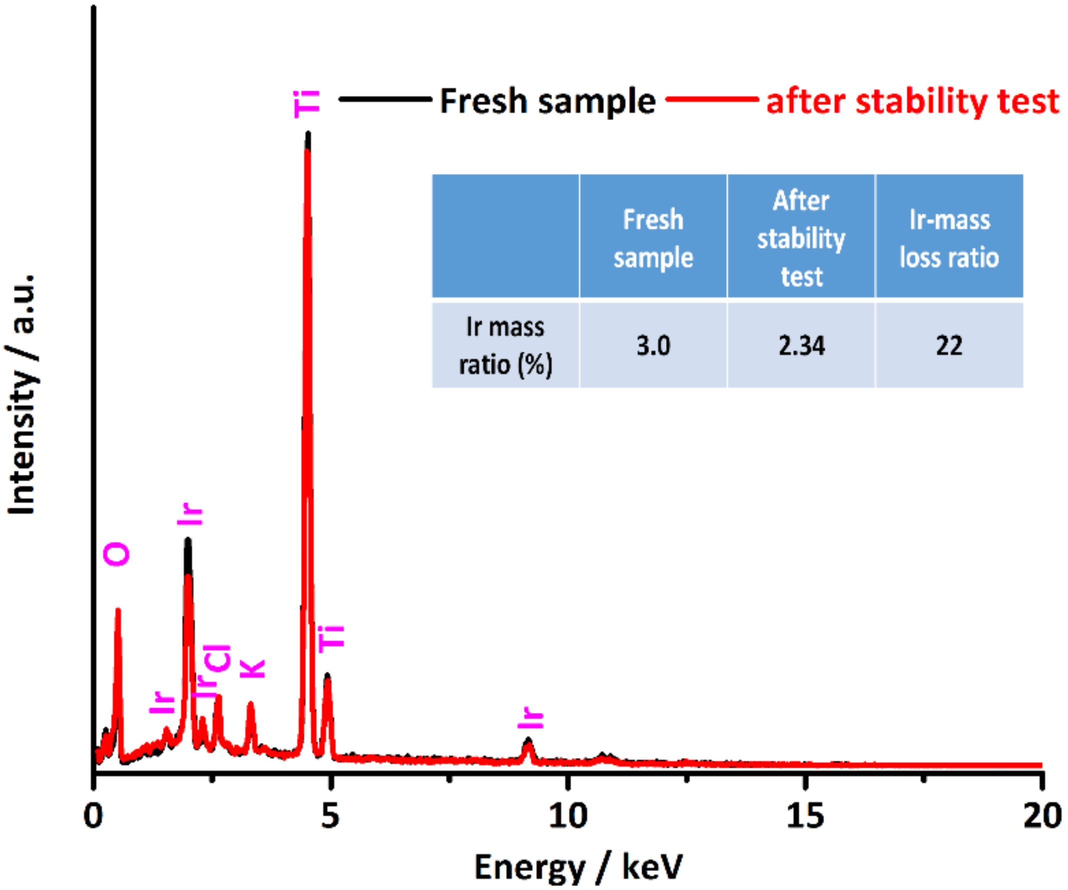

	Fresh sample	After stability test	Ir-mass loss ratio
Ir mass ratio (%)	3.0	2.34	22

Fig. S25 EDX spectra of H-Ti@IrO_x before and after the extended stability test at 200 mA cm^{-2} for 130 h, showing that only ca. 22 % of initial IrO_x lost during the stability test.

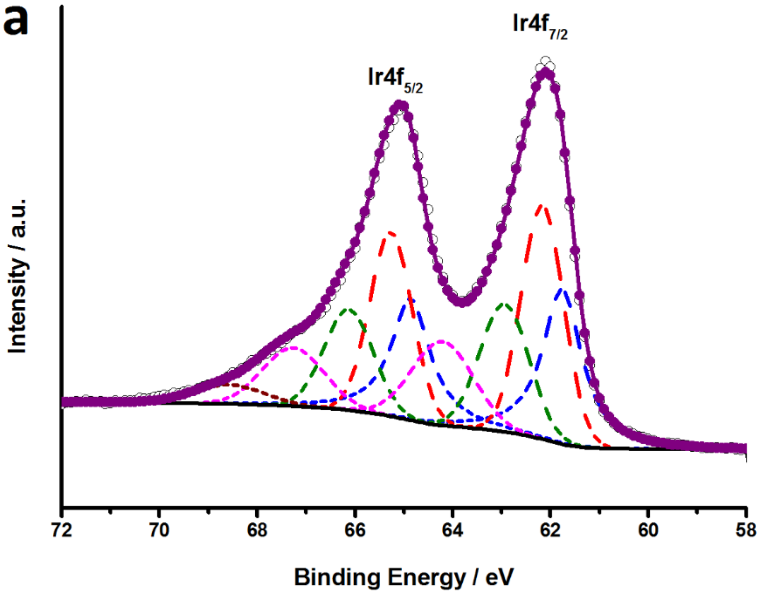

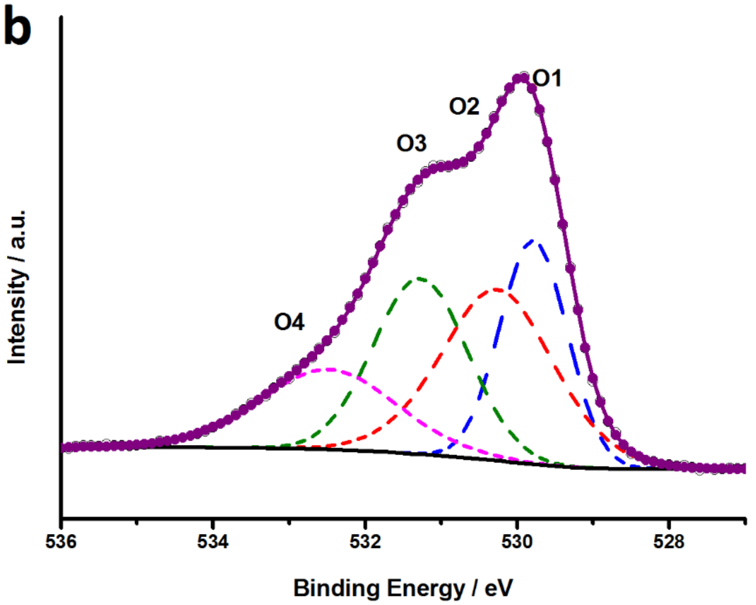

Fig. S26 (a) Ir 4f (Blue and red curves represent Ir^{IV} and Ir^{III}, respectively; olive, wine and orange curves represent Ir^{IV} satellite 1, satellite 2 and Ir^{III} satellite, respectively). (b) O 1s spectra of H-Ti@IrO_x after the extended stability test at 200 mA cm^{-2} for 130 h.

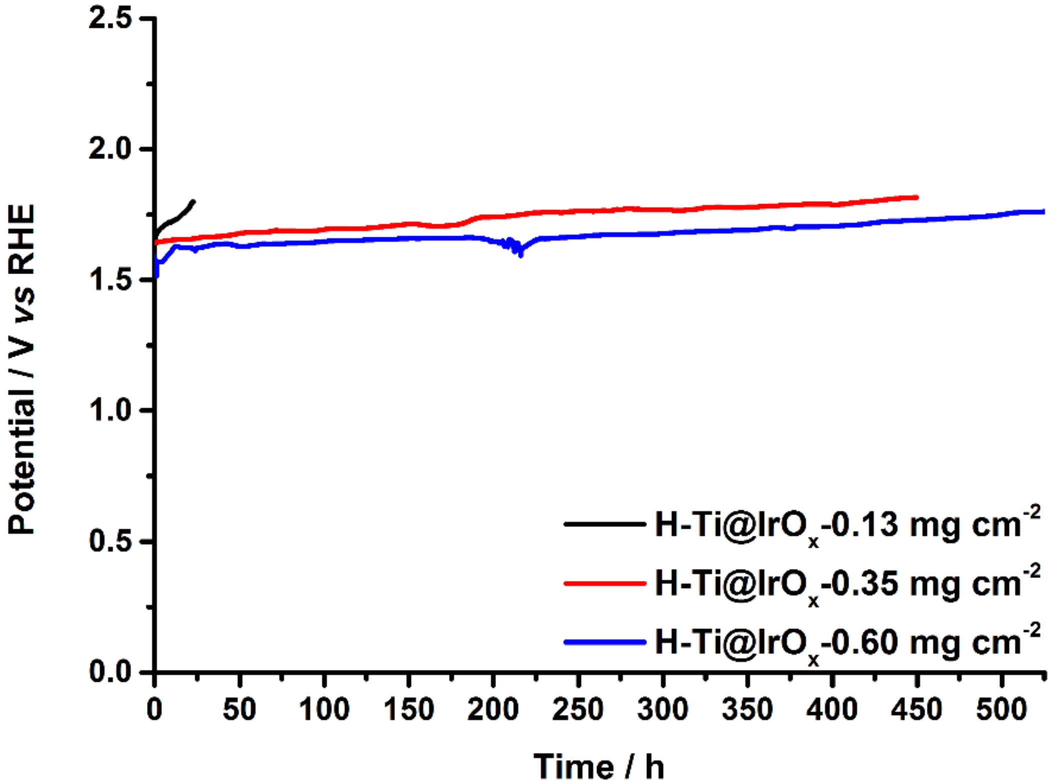

Fig. S27 Chronopotentiometric curves recorded at a constant current density of 200 mA cm^{-2} for H-Ti@IrO$_x$-0.13 mg cm^{-2}, H-Ti@IrO$_x$-0.35 mg cm^{-2} and H-Ti@IrO$_x$-0.60 mg cm^{-2}.

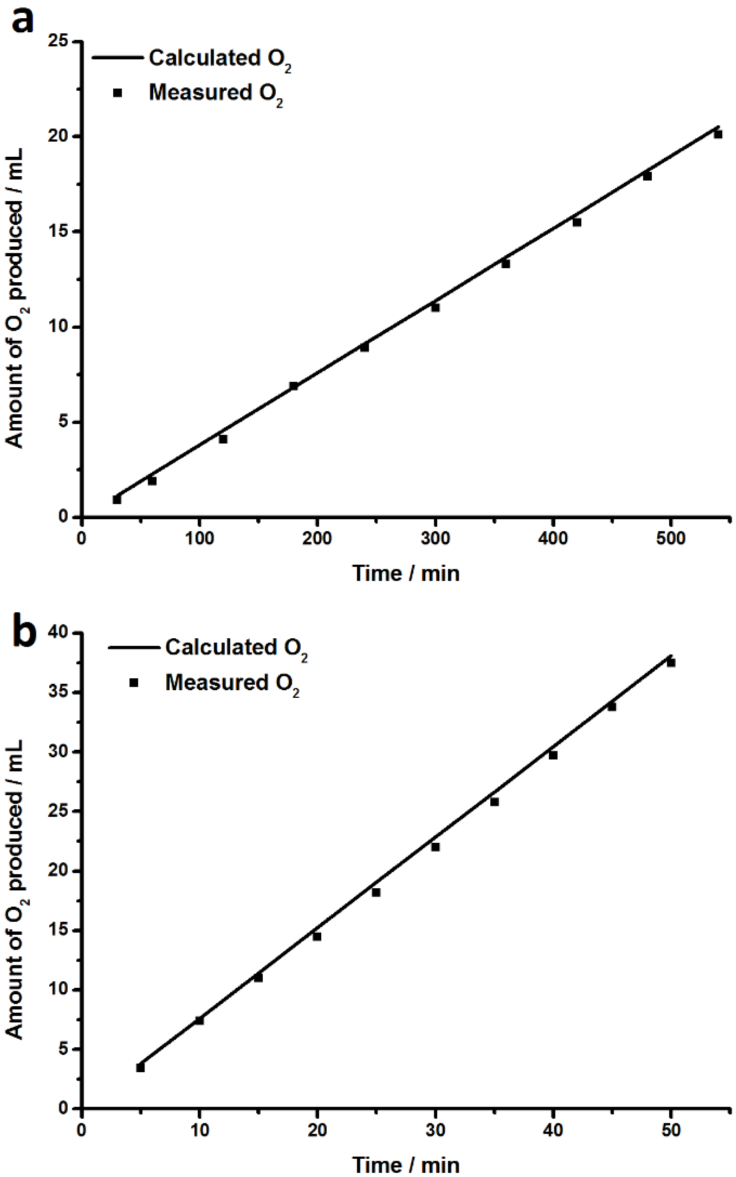

Fig. S28 Experimentally measured and calculated volumes of O_2 gas evolved from H-Ti@IrO$_x$ at a fixed current density of (a) 10 mA cm^{-2} and (b) 200 mA cm^{-2}. Electrolyte: 0.5 M H_2SO_4.

Supplementary tables

Table S1. Fitting parameters of O1s spectra of H-Ti@IrO$_x$, P-Ti@IrO$_x$, C@IrO$_x$, commercial IrO$_2$, H-Ti@IrO$_x$-air-0.5 h and H-Ti@IrO$_x$-air-5 h.

	O1	**O2**	**O3**	**O4**
H-Ti@IrO$_x$				
BE (eV)	529.8	530.4	531.4	532.7
Area (%)	33.0	37.0	18.5	11.5
FWHM (eV)	1.1	1.9	1.5	1.9
P-Ti@IrO$_x$				
BE (eV)	529.8	530.4	531.4	532.6
Area (%)	40.1	28.5	17.7	13.7
FWHM (eV)	1.0	1.9	1.9	2.1
C@IrO$_x$				
BE (eV)	529.8	530.4	531.4	532.6
Area (%)	15.4	34.4	25.1	25.1
FWHM (eV)	0.9	1.9	2.4	2.4
Commercial IrO$_2$				
BE (eV)	529.8	530.5	531.4	532.6
Area (%)	45.5	20.5	14.5	19.5
FWHM (eV)	0.8	1.4	1.7	2.9
H-Ti@IrO$_x$-air-0.5 h				
BE (eV)	529.8	530.3	531.3	532.3
Area (%)	28.3	32.6	18.2	20.9
FWHM (eV)	1.3	2.0	1.4	2.0
H-Ti@IrO$_x$-air-5 h				
BE (eV)	529.8	530.3	531.3	532.4
Area (%)	36.5	27.0	23.4	13.1
FWHM (eV)	1.2	1.2	1.9	2.5

BE: binding energy; FWHM: full width at half maximum.

Table S2. Fitting parameters of Ir 4f spectra of H-Ti@IrO$_x$, P-Ti@IrO$_x$, C@IrO$_x$, commercial IrO$_2$, H-Ti@IrO$_x$-air-0.5 h and H-Ti@IrO$_x$-air-5 h.

Catalysts	**Content of Ir species (%)**	
	Ir^{3+}	**Ir^{4+}**
H-Ti@IrO$_x$	56.4	43.6
P-Ti@IrO$_x$	45.1	54.9
C@IrO$_x$	53.2	46.8
Commercial IrO$_2$	36.8	63.2
H-Ti@IrO$_x$-air-0.5 h	48.2	51.8
H-Ti@IrO$_x$-air-5 h	40.8	59.2

Table S3. Fitting parameters of Ir 4f spectra of H-Ti@IrO$_x$, P-Ti@IrO$_x$, C@IrO$_x$, commercial IrO$_2$, H-Ti@IrO$_x$-air-0.5 h and H-Ti@IrO$_x$-air-5 h.

	Ir4f$_{7/2}$ Ir^{IV}	**Ir4f$_{5/2}$ Ir^{IV}**	**Ir4f$_{7/2}$ Ir^{IV} sat 1**	**Ir4f$_{5/2}$ Ir^{IV} sat 1**	**Ir4f$_{5/2}$ Ir^{IV} sat 2**	**Ir4f$_{7/2}$ Ir^{III}**	**Ir4f$_{5/2}$ Ir^{III}**	**Ir4f$_{7/2}$ Ir^{III} sat 1**	**Ir f$_{5/2}$ Ir^{III} sat 1**
H-Ti@IrO$_x$									
BE (eV)	61.7	64.8	62.9	66.1	68.4	62.1	65.2	64.1	67.2
Area (%)	15.3	11.9	11.7	9.3	2.6	19.8	15.7	7.9	5.8
FWHM (eV)	0.9	0.9	1.2	1.2	1.4	1.1	1.1	1.3	1.3
P-Ti@IrO$_x$									
BE (eV)	61.7	64.8	62.7	65.9	68.7	62.1	65.2	64.0	67.0
Area (%)	17.4	13.7	10.4	8.2	3.0	14.3	11.3	12.5	9.2
FWHM (eV)	0.7	0.7	1.1	1.1	1.8	0.8	0.8	1.7	1.7
C@IrO$_x$									
BE (eV)	61.7	64.8	62.9	66.0	68.8	62.1	65.2	64.1	67.1
Area (%)	11.5	9.2	17.0	13.4	2.5	13.1	10.2	13.4	9.7
FWHM (eV)	0.8	0.8	1.2	1.2	1.8	0.9	0.9	1.9	1.9
Commercial IrO$_2$									
BE (eV)	61.6	64.7	63.0	66.1	68.2	62.1	65.2	64.1	67.1
Area (%)	21.3	16.8	9.0	7.0	2.8	12.4	9.6	12.8	8.3
FWHM (eV)	0.7	0.7	1.2	1.2	1.3	1.1	1.1	1.3	1.3
H-Ti@IrO$_x$-air-0.5 h									
BE (eV)	61.7	64.8	62.9	66.1	68.9	62.2	65.3	64.0	67.1
Area (%)	14.4	11.4	12.9	10.2	2.0	13.4	10.5	14.1	11.1
FWHM (eV)	1.2	1.2	1.4	1.4	1.8	1.2	1.2	1.9	1.9
H-Ti@IrO$_x$-air-5 h									
BE (eV)	61.7	64.8	62.9	66.0	68.9	62.2	65.3	63.9	67.1
Area (%)	18.4	14.5	10.8	8.5	1.3	12.7	10.1	13.2	10.5
FWHM (eV)	1.1	1.1	1.2	1.2	1.5	1.1	1.1	1.8	1.8

BE: binding energy; FWHM: full width at half maximum.

References

[S1] W. J. Zhou, X. J. Liu, Y. H. Sang, Z. H. Zhao, K. Zhou, H. Liu and S. W. Chen, *ACS Appl. Mater. Interfaces,* 2014, **6**, 4578-4586.

[S2] L. L. Zhao, Q. Cao, A. L. Wang, J. Z. Duan, W. J. Zhou, Y. H. Sang and H. Liu, *Nano Energy,* 2018, **45**, 118-126.

[S4] X. G. Wang, W. Li, D. H. Xiong, D. Y. Petrovykh and L. F. Liu, *Adv. Funct. Mater.,* 2016, **26**, 4067-4077.

[S5] V. V. Gorodetskii and V. A. Neburchilov, *Russ. J. Electrochem.,* 2003, **39**, 1116-1123.

[S6] S. Geiger, O. Kasian, B. R. Shrestha, A. M. Mingers, K. J. J. Mayrhofer and S. Cherevko, *J. Electrochem. Soc.*, 2016, **163**, F3132-F3138.

[S6] G. Kresse and J. Furthmüller, *Phys. Rev. B,* 1996, **54**, 11169-11186.

[S7] J. P. Perdew, K. Burke and M. Ernzerhof, *Phys. Rev. Lett.,* 1996, **77**, 3865-3868.

[S8] P.E. Blöchl, *Phys. Rev. B,* 1994, **50**, 17953-17979.

[S9] Z. Alexandra and A. Vitaly, *ACS Catal.*, 2020, **10**, 3650-3657.

[S10] J. K. Nørskov, J. Rossmeisl, A. Logadottir, L. Lindqvist, J. R. Kitchin, T. Bligaard and H. Jónsson, *J. Phys. Chem. B,* 2004, **108**, 17886-17892.

[S11] C. C. L. McCrory, S. H. Jung, I. M. Ferrer, S. M. Chatman, J. C. Peters and T. F. Jaramillo, *J. Am. Chem. Soc.,* 2015, **137**, 4347-4357.